The prolactin receptor scaffolds Janus kinase 2 via co-structure formation with phosphoinositide-4,5-bisphosphate

Raul Araya-Secchi[1,2], Katrine Bugge[3#], Pernille Seiffert[3#], Amalie Petry[4], Gitte W. Haxholm[3], Kresten Lindorff-Larsen[3], Stine F. Pedersen[4*], Lise Arleth[1*] and Birthe B. Kragelund[3*],

[1]Structural Biophysics, Section for Neutron and X-ray Science, Niels Bohr Institute, University of Copenhagen, 2100 Copenhagen, Denmark.
[2]Facultad de Ingenieria Arquitectura y Diseño, Universidad San Sebastian, Bellavista 7, Santiago, Chile.
[3]Structural Biology and NMR Laboratory (SBiNLab), Department of Biology, University of Copenhagen, 2200 Copenhagen, Denmark.
[4]Section for Cell Biology and Physiology, Department of Biology, University of Copenhagen, 2200 Copenhagen N, Denmark

#contributed equally

*Corresponding author: bbk@bio.ku.dk.
Correspondence also to arleth@nbi.ku.dk and sfpedersen@bio.ku.dk

Running title: Co-structure formation by PRLR, JAK2 and PI(4,5)P_2

Abstract

Class 1 cytokine receptors transmit signals through the membrane by a single transmembrane helix to an intrinsically disordered cytoplasmic domain that lacks kinase activity. While specific binding to phosphoinositides has been reported for the prolactin receptor (PRLR), the role of lipids in PRLR signalling is unclear. Using an integrative approach combining NMR spectroscopy, cellular signalling experiments, computational modelling and simulation, we demonstrate co-structure formation of the disordered intracellular domain of the human PRLR, the membrane constituent phosphoinositide-4,5-bisphosphate (PI(4,5)P_2) and the FERM-SH2 domain of the Janus kinase 2 (JAK2). We find that the complex leads to accumulation of PI(4,5)P_2 at the transmembrane helix interface and that mutation of residues identified to interact specifically with PI(4,5)P_2 negatively affects PRLR-mediated activation of signal transducer and activator of transcription 5 (STAT5). Facilitated by co-structure formation, the membrane-proximal disordered region arranges into an extended structure. We suggest that the co-structure formed between PRLR, JAK2 and PI(4,5)P_2 locks the juxtamembrane disordered domain of the PRLR in an extended structure, enabling signal relay from the extracellular to the intracellular domain upon ligand binding. The co-structure exists in different states which could be relevant for turning signalling on and off. Similar co-structures may be relevant for other non-tyrosine kinase receptors.

Keywords: IDP, NMR, simulation, prolactin receptor, JAK2, single-pass transmembrane receptors, PI(4,5)P_2,

Introduction

Cytokine receptors are transmembrane glycoproteins that bind cytokines on the cell-surface and transduce signals across the membrane to the interior of the cell. This, in turn, activates signalling pathways leading to multiple outcomes including induction of immune responses, cell proliferation, altered metabolism and differentiation (Brooks et al., 2016). Class 1 cytokine receptors constitute a subclass of receptors that transverse the membrane by a single α-helical transmembrane domain (TMD) (Brooks et al., 2016), separating a folded extracellular domain (ECD) from a disordered intracellular domain (ICD). The prolactin (PRL) receptor (PRLR) represents one of the structurally most simple cytokine receptor (***Figure 1***). Signaling by the PRLR/PRL complex is implicated in the regulation of more than 300 biological functions in vertebrates (Bole-Feysot et al., 1998), and its function is especially well-known for its essential role in mammary gland development and lactation (Hannan et al., 2022). Apart from this, deregulation of PRLR/PRL signalling is associated with several pathologies in humans of which hyperprolactinemia resulting in reproductive failure is best described (Bachelot and Binart, 2007; Newey et al., 2013). Deregulation of PRLR/PRL signaling is linked to other diseases and, although still debated, suggested to be implicated in the development and progression of prostate (Sackmann-Sala and Goffin, 2015) and breast (Clevenger and Rui, 2022) cancers.

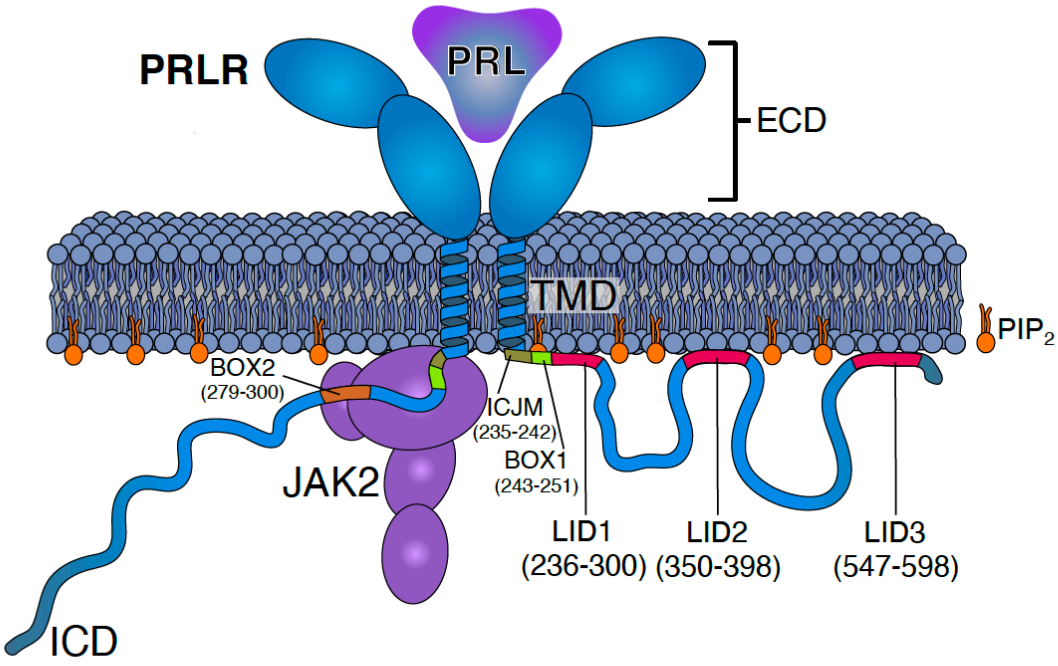

Fig. 1: Schematics of the PRLR:PRL:JAK2 complex in the membrane. The PRLR is shown in light blue, the PRL as a dark blue triangle, the PRLR-ICD as a disordered chain and JAK2 in purple. The lipid PI(4,5)P_2 is shown in orange. The intracellular juxtamembrane (ICJM) region and BOX1 of PRLR-ICD are highlighted in green nuances, while the three LIDs as defined in Haxholm et al., (Haxholm et al., 2015) are highlighted in red. For simplicity only one of the two ICDs is shown associated with JAK2.

For cytokine receptors, signal transduction through the membrane is received by an ICD, which is intrinsically disordered and lacks kinase activity (Haxholm et al., 2015). Thus, association of

83 auxiliary kinases is mandatory for signalling, with the Janus kinases (JAK1–3) and the tyrosine kinase
84 TYK2 being the most thoroughly described (Brooks et al., 2016; Morris et al., 2018). A proline-rich
85 region constituting the so-called BOX1 motif close to the membrane, as well as a second hydrophobic
86 motif termed BOX2, are known to be essential for JAK binding (***Figure 1***) (Ferrao et al., 2018;
87 Rowlinson et al., 2008). However, although progress has been made in the molecular understanding
88 of cytokine binding and despite several structures of folded ECDs (Broutin et al., 2010; de Vos et al.,
89 1992), TMDs (Bocharov et al., 2018; Bugge et al., 2016), a complete receptor (Kassem et al., 2021)
90 and a receptor ICD in complex with JAK1 (Glassman et al., 2022) have emerged, it is still not clear
91 how the signal inside the cell is received by the disordered region to elicit and in turn control signal
92 transduction.
93
94 A subset of class 1 cytokine receptors form homodimers and trimeric complexes with their ligands,
95 with the main dimerization occurring in the TMDs (Brooks et al., 2014; Brown et al., 2005; Gadd
96 and Clevenger, 2006; Kubatzky et al., 2001; Seubert et al., 2003). This group includes the growth
97 hormone receptor (GHR), the erythropoietin receptor (EPOR) and the PRLR, which have become
98 well-established paradigmatic models. Recently, signal transduction by the GHR has been suggested
99 to occur via a rotation of the transmembrane helices within the dimer leading to a subsequent
100 separation of the ICDs (Brooks et al., 2014; Brown et al., 2005). A torque is hereby exerted on the
101 associated JAK2s, which is thought to relieve inhibition by the pseudokinase domains, initiating
102 signalling. The ICDs of these receptors have been shown to be highly disordered (Haxholm et al.,
103 2015), a feature which is preserved in models of the PRLR (Bugge et al., 2016) and in the structure
104 of the full-length GHR in nanodiscs (Kassem et al., 2021). This brings forward the question of how
105 signalling is orchestrated by disorder and how a disordered linker region between the TMD and the
106 region bound to the kinases can communicate and transduce information.
107
108 For both the PRLR and the GHR, lipid interaction domains (LID) with affinity for negatively charged
109 lipids have been identified in their ICDs (Haxholm et al., 2015). Common to both receptors is that
110 they contain a LID proximal to the membrane, directly overlapping with the JAK2 interaction sites,
111 BOX1 and BOX2 (Seiffert et al., 2020). Using nuclear magnetic resonance (NMR) spectroscopy we
112 identified three LIDs in the PRLR-ICD termed LID1, LID2 and LID3 (***Figure 1***) (Haxholm et al.,
113 2015) and using lipid dot-blots we showed that the PRLR-ICD has variable affinities for different
114 membrane constituents, with a distinct preference for phosphoinositides (PIs), particularly
115 phosphoinositide-4,5-bisphosphate (PI(4,5)P_2) (Haxholm et al., 2015). PIs are important constituents
116 of the membrane and play key roles in signalling, both as membrane interaction partners that can be
117 specifically modulated by phosphorylation (Carracedo and Pandolfi, 2008), and as secondary
118 messengers (McLaughlin et al., 2002; Suh and Hille, 2005). Indeed, some single-pass receptors
119 contain conserved anionic lipid interaction sites close to the membrane (Hedger et al., 2015a) and
120 increasing evidence suggest lipid interaction to take on important regulatory roles (McLaughlin et al.,
121 2005; Metcalf et al., 2010). Recently, PI(4,5)P_2 was shown to regulate the epidermal growth factor
122 receptor (EGFR) dimer/monomer equilibrium with a possible positive feedback loop through the
123 activation of the phospholipase C (PLC) – diacylglycerol (DAG)-IP_3 pathways, leading to conversion
124 of PI(4,5)P_2 to PI(3,4,5)P_3 and hence depletion of PI(4,5)P_2 from the membrane (Maeda et al., 2018).

Similar depletion of PI(4,5)P_2 from the plasma membrane has been noted under hypoxia (Lu et al., 2022). For class 1 cytokine receptors the role of PIs in signalling is less clear.

In a cellular context, signalling-related proteins can be membrane anchored through modifications such as acylation (Patwardhan and Resh, 2010; Rawat et al., 2013; Rawat and Nagaraj, 2010) or via designated lipid-binding domains. This includes the four point-1, ezrin, radixin moesin (FERM) domain of radixin, focal adhesion kinase (FAK) and the protein tyrosine phosphatase L1 (PTPL1) (Bompard et al., 2003; Feng and Mertz, 2015; Hamada et al., 2000), the SH2 domains of the Src family kinases (Park et al., 2016; Sheng et al., 2016) and the FERM-SH2 domain of merlin (Mani et al., 2011). Thus, kinases and receptors can co-localize at the plasma membrane without necessarily being bound within a complex. It is, however, unclear whether such membrane co-localisation has any functional consequences, such as enhancing signalling speed, and whether the membrane may act as an additional scaffolding platform that enhance binding affinity via restriction in the two-dimensional plane.

For the PRLR it is still not clear whether and if so how interactions between the ICD and the membrane impact signal transduction and association with JAK2. Nor is it understood how structural disorder can relay and transmit information from the TMD to initiate signalling. To shed light on the molecular details underlying a potential interplay between the receptor, membrane and kinase we focused on the human PRLR and its LID1 closest to the membrane. Using an integrative approach combining NMR spectroscopy, cell biology and computational modelling, we demonstrate the formation of a co-structure comprised of the disordered PRLR-ICD, the membrane constituent PI(4,5)P_2 and the FERM-SH2 domain of the JAK2. Facilitated by this co-structure, the disordered region closest to the membrane forms an extended structure, which we suggest stabilizes the disordered domain, allowing signal relay from the extracellular to the intracellular domain.

Results

LID1 is disordered in solution and when tethered to the transmembrane helix

Membrane interactions by PRLR-ICD have previously been studied in the absence of anchoring to the TMD defining three LIDs, with LID1 closest to the membrane (Haxholm et al., 2015). Since tethering would increase the local concentrations of the membrane and the ICD, this could affect affinity, complex lifetime as well as the degree by which structure formation would be captured. In the present study, we therefore recombinantly expressed the TMD (residues 211–235 with numbering corresponding to the processed protein) with five residues added at the two termini ($TMD_{F206-V240}$), and the TMD with the first 35 residues of LID1, TMD-$ICD_{F206-S270}$ (***Figure 2A***). We then examined their structural propensities in detergents and in small unilamellar vesicles (SUVs) by NMR spectroscopy. In 1,2-dihexanoyl-sn-glycero-3-phosphocholine (DHPC) micelles, most of the TMD resonances of the $TMD_{F206-V240}$ and TMD-$ICD_{F206-S270}$ variants were readily superimposable in the $^{15}N,^{1}H$-HSQC spectra (***Figure 2 - figure supplement 1***), suggesting that the conformation of the TMD was not affected by the presence of the ICD. For the TMD-$ICD_{F206-S270}$, C^{α} NMR resonances were collected for most of the disordered region, while backbone carbon resonances were broadened beyond detection for the TMD and the region G236-P246 immediately following it (***Figure 2B)***. This

may suggest that the first ten residues of the ICD interact with or are buried in the micelles, or are affected by the overall slower tumbling of the micelle. We assigned the backbone nuclei of the detectable resonances of TMD-ICD$_{F206-S270}$ in DHPC micelles and compared the secondary chemical shifts (SCS) to those of the ICD alone (ICD$_{G236-Q396}$) (***Figure 2C***). Whereas the region of the ICD that is undetected in TMD-ICD$_{F206-S270}$ formed transient extended structures in the absence of the TMD, the observable parts were highly similar suggesting lack of structure induction by TMD tethering or the micelles. In 1-palmitoyl-2-oleoyl-sn-glycero-3-phosphocholine (POPC) SUVs, only the resonances of the most C-terminal residues of TMD-ICD$_{F206-S270}$ were detectable; however, the chemical shifts suggested that the residues were disordered (***Figure 2 – figure supplement 2***). Taken together, these results suggest that most of the ICD residues remain disordered when tethered to the TMD and in the presence of a neutral membrane mimetic.

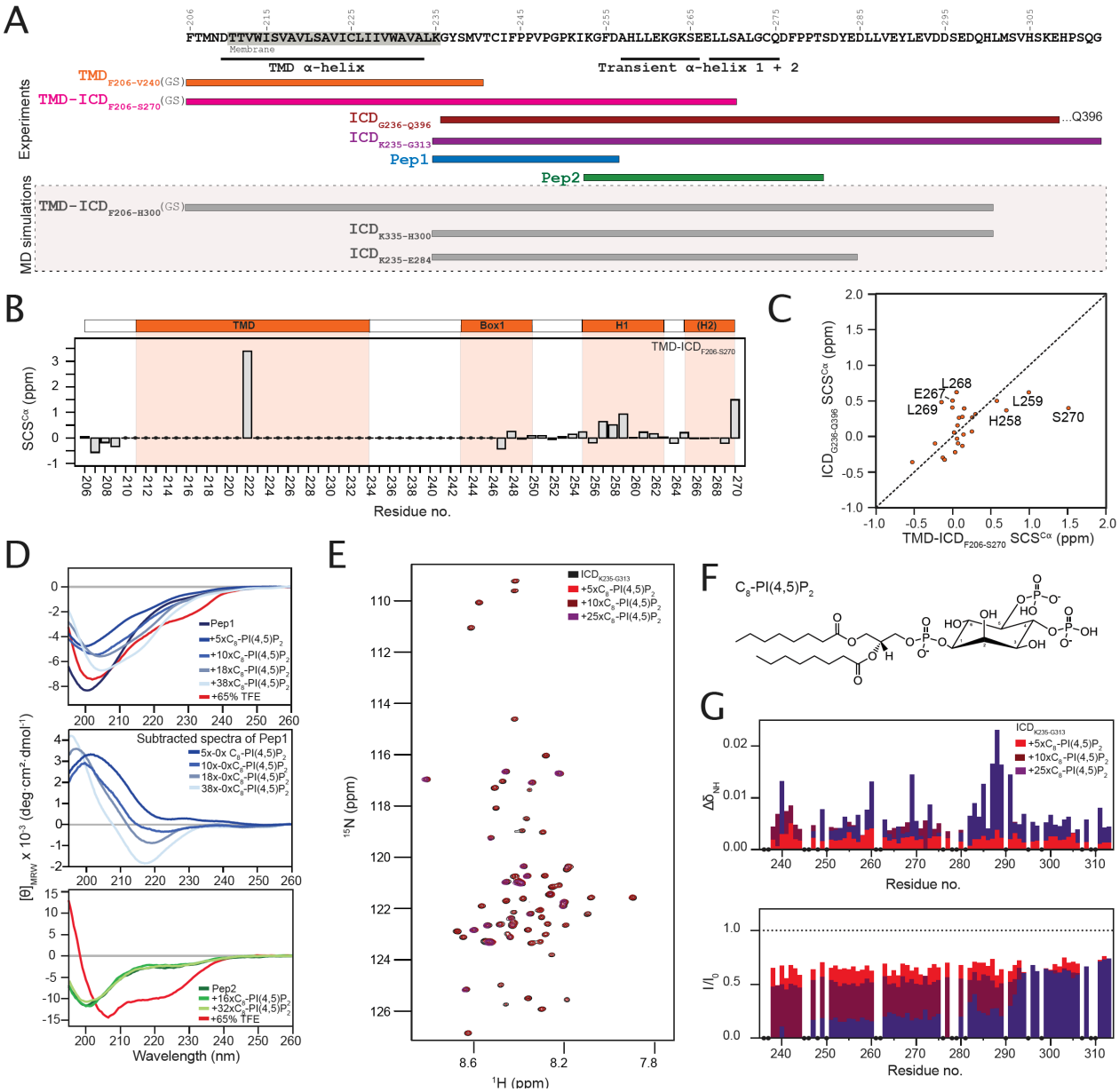

Fig. 2: The ICJM region of the PRLR interacts with PI(4,5)P_2. A) Overview of investigated PRLR variants. **B)** Secondary chemical shifts (SCSs) of TMD-$ICD_{F206-S270}$ reconstituted in DHPC micelles. **C)** Correlation plot of the SCSs of $ICD_{G236-Q396}$ plotted against those of TMD-$ICD_{F206-S270}$. **D) Top**: Far-UV CD spectra of Pep1 titrated with C_8-PI(4,5)P_2 or in 65% TFE. **Middle:** Far-UV CD spectra of Pep1 in the presence of 5x-38x C_8-PI(4,5)P_2 subtracted with the spectrum of Pep1 in the absence of C_8-PI(4,5)P_2. **Bottom**: Far-UV CD spectra of Pep2 titrated with C_8-PI(4,5)P_2 or in 65% TFE. **E)** ^{15}N,^{1}H-HSQC spectra of ^{15}N-$ICD_{K235-G313}$ titrated with 5x, 10x and 25x molar excess of C_8-PI(4,5)P_2. **F) Structure of** C_8-PI(4,5)P_2 **G)** Backbone amide chemical shift perturbations (CSPs) and peak intensity changes upon addition of C_8-PI(4,5)P_2 to ^{15}N-$ICD_{K235-G313}$ plotted against residue number.
Figure supplement 1: *^{15}N, ^{1}H-HSQC spectra of A) $TMD_{F206-V240}$ and TMD-$ICD_{F206-S270}$ in DHPC micelles, and (B) TMD-$ICD_{F206-S270}$ in POPC SUVs.*
Figure supplement 2: *C^{α} secondary chemical shifts of $ICD_{G236-Q396}$*

LID1 binds PI(4,5)P_2 in the juxtamembrane region forming extended structures

PRLR-ICD has previously been shown to bind PI(4,5)P_2 (Haxholm et al., 2015), suggesting that this lipid could modulate membrane affinity and the structural properties of the PRLR-ICD. To separate headgroup effects from lipid bilayer surface effects, we used a short-chain C_8-PI(4,5)P_2, which has a high critical micelle concentration (CMC) of 2 mM (Goñi et al., 2014) and analysed the structural changes by circular dichroism (CD) and NMR spectroscopy at concentrations below the CMC (Goñi et al., 2014) to identify the binding site.

^{15}N-labelled $ICD_{K235-G313}$ covering LID1 (***Figure 1***) was titrated with C_8-PI(4,5)P_2 and binding was assessed by ^{1}H-^{15}N-HSQC spectra (***Figure 2E,F***). The chemical shift perturbations (CSPs) were modest whereas substantial intensity changes were observed throughout the chain, supporting a direct interaction between the ICD and lipids. The resonances from G236-F244 completely disappeared suggesting exchange on an intermediate NMR timescale, while intensities were substantially reduced in the V247-S290 region (***Figure 2F***). From this region and to the C-terminus, only moderate intensity changes were observed (***Figure 2F***). These findings suggest that the primary PI(4,5)P_2 binding site is located closest to the membrane in what we define as the intracellular juxtamembrane (ICJM) region (K235-C242). The ICJM is located N-terminally to the BOX1 motif ($_{243}$IFPPVPGPK$_{251}$ (UNIPROT); $_{245}$PPVPGPK$_{251}$ (elm.eu.org)).

As the resonance-broadening precluded observation of the bound state, two overlapping peptides, Pep1 (K235-D256) and Pep2 (K253-T280), were constructed and evaluated by CD spectroscopy. In isolation, the peptides were disordered as judged by the negative ellipticity at 200 nm in their far-UV CD spectra (***Figure 2D***). Pep1 and Pep2 were titrated with C_8-PI(4,5)P_2 and the structural changes monitored (***Figure 2D***). For Pep2, the far-UV CD signal was unaffected by the presence of C_8-PI(4,5)P_2. In contrast, for Pep1, large spectral changes were seen, which were unrelated to helix formation. Subtracting the spectra in the presence and absence of C_8-PI(4,5)P_2, revealed a negative ellipticity at 218 nm, showing that when bound to C_8-PI(4,5)P_2, a distinct extended (strand-like structure) signature was seen (***Figure 2D***). This suggests that this region of LID1 changes its conformational properties upon binding to C_8-PI(4,5)P_2. We evaluated the intrinsic helical propensities of the two ICD segments by exposure to high trifluorethanol (TFE) concentrations. Here,

223 Pep2 was readily able to form helical structure as expected from the presence of two transient helices
224 (Haxholm et al., 2015) (***Figure 2D, top***), whereas Pep1 was not (***Figure 2D, bottom***).
225
226 In summary, LID1 of the PRLR-ICD interacts with PI(4,5)P_2,with the primary interaction site located
227 in the K235-S290 region. Headgroup interaction was dominantly located to the region K235-D256
228 constituting the ICJM and the BOX1 motif and this interaction induced the formation of a regional
229 extended structure in the PRLR-ICD.
230
231 **LID1 has specific PI(4,5)P_2 contacts which drive PI(4,5)P_2 recruitment**
232 To obtain a more detailed characterization of the behaviour of the disordered PRLR-ICD near lipid
233 bilayers, as well as the effect of different anionic lipid headgroups in these, we turned to molecular
234 simulations. Here, we focused on the LID1 (K235-H300), alone and in context of TMD, and first
235 placed a coarse-grained (CG) model of the TMD-$ICD_{F206-H300}$ in three different mixed-membrane
236 systems. These contained an upper leaflet consisting of 100% POPC and lower leaflets composed of
237 either a 70:30 molar ratio mixture of POPC:1-palmitoyl-2-oleoyl-sn-glycero-3-phospho-L-serine
238 (POPS), or a 90:5:5 or 80:10:10 mixture of POPC:POPS:PI(4,5)P_2 (***Figure 3***). Since the Martini
239 forcefield may produce unrealistically collapsed disordered regions, increasing the strength of the
240 protein-water interactions by 8–10% has provided satisfactory results when applied to the simulation
241 of other disordered regions or multidomain proteins (Thomasen et al., 2022). Thus, the simulations
242 were run using a modified version of the Martini3 forcefield with a 10% increase in the strength of
243 the protein-water interactions. For comparison, similar simulations were done using the Martini2
244 forcefield (***Figure 3 – figure supplement 1***).
245
246 We first analysed the dynamics of the LID1 during the simulations focusing on the pattern of protein-
247 lipid contacts. Here, we measured the number of protein-lipid contacts focusing either on interactions
248 between the protein and lipid headgroups (***Figures 3A-C***) or the protein and lipid acyl chains (***Figures***
249 ***3D-F***). In both cases we determined the fraction of the simulation time that the protein and different
250 parts of the lipid were within 7Å of each other. In general, we observed that residues in the N-terminal
251 part of the LID1 (K235 - D255), which includes the ICJM and BOX1, established contacts with the
252 bilayer in all three membrane systems. Furthermore, a hydrophobic region rich in prolines (V240–
253 P250) made consistent contacts with the acyl-chains and much more than to the headgroups,
254 indicating penetration into the lower-leaflet. Similar behaviour has been reported with CG-MD
255 simulations for the juxtamembrane region of other single-pass transmembrane receptors (Hedger et
256 al., 2015b). For PRLR, the pattern of interaction was independent on the lipid composition, at least
257 in terms of protein-POPC contacts, and the region interacting with the lipids was similar in all three
258 membrane systems (***Figure 3***).
259
260 Although the extent and pattern of protein-lipid interactions appeared constant, a striking observation
261 was made in both systems containing PI(4,5)P_2. Here, protein-lipid interactions between residues
262 K235 and K253 and PI(4,5)P_2 were present during a large fraction (≥50%) of the simulations, despite
263 PI(4,5)P_2 being present at only 5% or 10% of the total lipids (***Figures 3 BC, EF***). This was also
264 observed in simulations with the Martini2 forcefield, in which the LID1 promptly collapsed in a

globular and unstructured coil (***Figure 3 – figure supplement 1 BC***). This suggested that PI(4,5)P_2 spontaneously assembled, or in other ways become concentrated around the TMD-$ICD_{F206-H300}$. The computed average density maps for PI(4,5)P_2 indeed showed that PI(4,5)P_2 formed a microdomain around the TMD (***Figure 3H***). The low frequency of contacts between the protein and POPS suggests that POPS did not accumulate or compete with PI(4,5)P_2 for binding to the TMD-$ICD_{F206-H300}$, further supporting the preference for PI(4,5)P_2 observed earlier (Haxholm et al., 2015). Similar preference was also observed with 5% PI(4,5)P_2 (***Figure 3 – figure supplement 1D***) as well as with Martini2 (***Figure 3 – figure supplement 1E-F***).

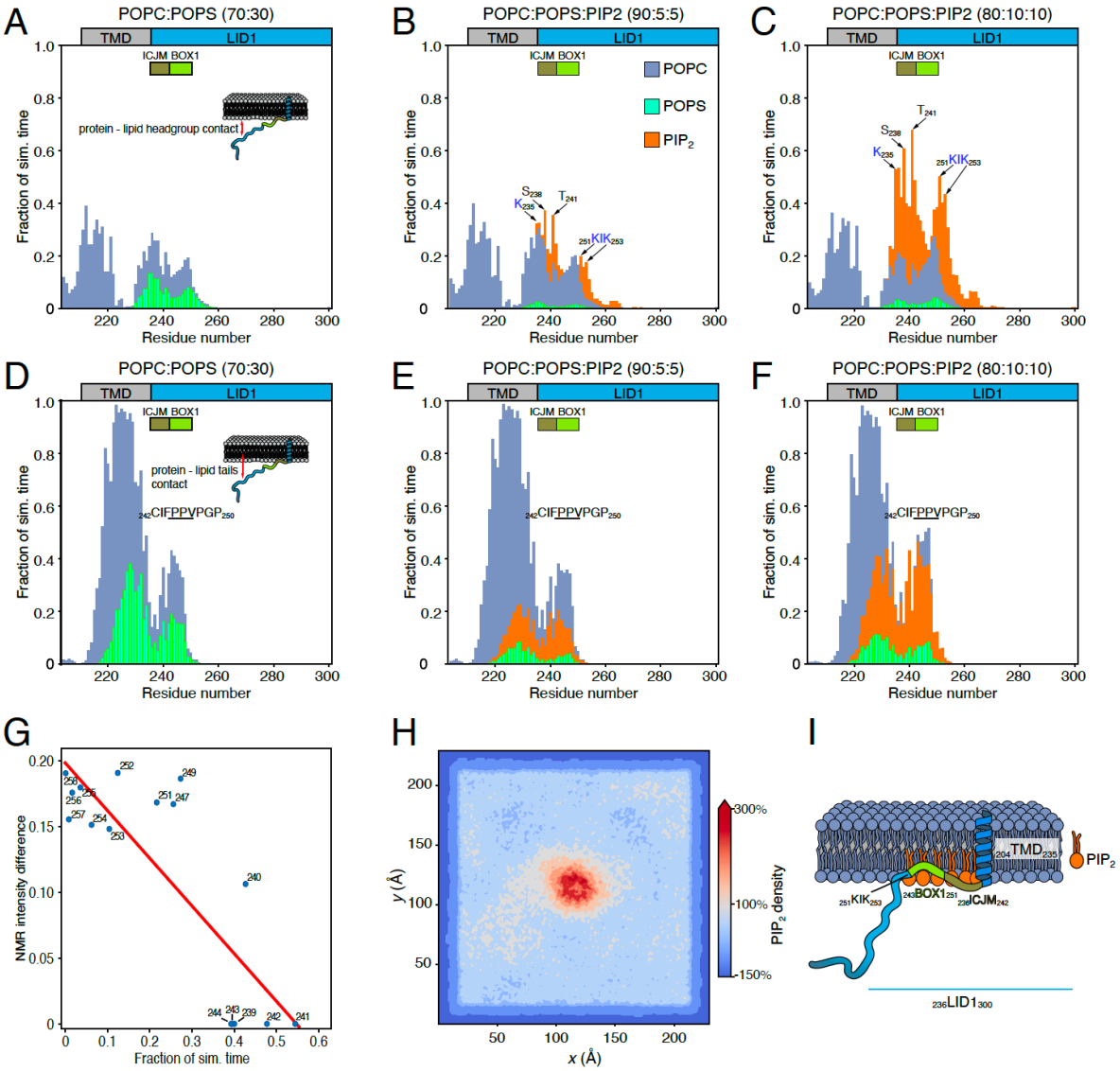

Fig. 3. Protein – lipid interactions of PRLR-ICD_{LID1} obtained from CG-MD simulations. **(A-F)** Protein – lipids contact histograms for PRLR-ICD_{LID1} and **A,D**) POPC:POPS(70:30), **B,E)** POPC:POPS:PI(4,5)P_2 (90:5:5) and **C,F)** POPC:POPS:PI(4,5)P_2 (80:10:10). A contact is counted if the distance between the backbone beads of the protein is ≤ 7 Å from the head-group beads of the lipids (A-C) or if the distance between the backbone bead of the protein is ≤ 7 Å from the acyl-chain bead of the lipids (D-F). **G)** Correlation between the change in NMR signal and the PRLR-ICD_{LID1} – PI(4,5)P_2 contact frequency from the PRLR-ICD_{LID1} + POPC:POPS:PI(4,5)P_2 (80:10:10) system. Pearson correlation

coefficient of -0.83 with $p = 7.3x10^{-5}$ and R^2= 0.7. **H)** Average PI(4,5)P_2 density map (*xy*-plane) taken from the PRLR-ICD_{LID1} + POPC:POPS:PI(4,5)P_2 (80:10:10) simulation. The map is colored according to the enrichment/depletion percentage with respect to the average density value. **I)** Schematic representation of how the interactions and the embedment into the membrane of PRLR contribute to the co-structure formation. The data from the simulations corresponds to those of the production stage (see methods).

Figure supplement 1: *Protein – lipid interactions of PRLR-ICD_{LID1} obtained from CG-MD simulations using the martini 2.2 forcefield*

A more detailed analysis of LID1-PI(4,5)P_2 contacts revealed a preference for certain residues, shown as peaks in the protein-headgroup contact profiles. In particular K235, S238, T241, and K251 and K253, which define a KIK motif suggested as a PI(4,5)P_2 binding motif (Kjaergaard and Kragelund, 2017), engaged in highly populated contacts (***Figure 3BC***). The pattern of contacts was not affected by PI(4,5)P_2 concentration; however, the frequency of contacts almost doubled as a result of the increase from 5% to 10% of PI(4,5)P_2. It appears that the penetration of and stabilization by hydrophobic residues in the ICJM and BOX1facilitate the approximation of the KIK motif to the PI(4,5)P_2 headgroups . Contributions from other positively charged residues such as K262 and K264 were very small. To validate the observations from the simulations, we compared the pattern of protein:PI(4,5)P_2 interactions observed in the NMR experiments to those from the simulations containing PI(4,5)P_2 (***Figure 3G***). A clear correlation between loss of NMR signal and high frequency of protein-PI(4,5)P_2 and POPC/POPS contacts in the 80:10:10 simulation was observed, reinforcing that the simulations are able to capture the specificity of protein-PI(4,5)P_2 interactions. Furthermore, both experiments (***Figure 2***) and simulations (***Figure 3***) show that the LID1 residues that help bind specifically to PI(4,5)P_2-containing membranes overlap with those that are involved in binding to JAK2.

In summary, the CG-simulations of TMD-$ICD_{F206-H300}$ near lipid membranes showed accumulation of PI(4,5)P_2 around the TMD and the N-terminus of LID1 involving the ICJM and BOX1. The residues made contact with the membrane independently of lipid type, with BOX1 residues acting as a tether by penetrating the headgroups. This tethering keeps positively charged residues, such as K251 and K253, near the membrane. This may be the driver for PI(4,5)P_2 recruitment, enhanced by higher PI(4,5)P_2 concentration. Intriguingly, we observed that the same regions involved in JAK2 binding (BOX1), also play roles in membrane association and lipid recruitment.

JAK2-FERM-SH2 and PRLR-ICD_{LID1} form co-structures with PI(4,5)P_2 on membranes

It has been suggested that JAK2 and PRLR interact constitutively in cells (Campbell et al., 1994; Rui et al., 1994) although recent data for the GHR have shown that the Src family kinase Lyn competes for this site (Chhabra et al., n.d.). Thus, given our observations that residues from LID1 form lipid-specific contacts with the membrane constituents using the same region covering the binding interface with the FERM domain of JAK2, we decided to explore the structure and dynamics of the JAK2(FERM-SH2):PRLR(LID1) complex near lipid bilayers (***Figure 4***). To do so, an atomistic model of the complex of a smaller region of PRLR-$ICD_{K235-E284}$ bound to the JAK2-FERM-SH2 domains (residues P37 to T514) was built, taking advantage of crystal structures of JAK2-FERM-SH2 and of JAK1-FERM-SH2 and TYK2-FERM-SH2 bound to analogous fragments of the ICDs of

the interferon λ- and α-receptors (IFNLR1 and IFNAR1), respectively. This model was used to perform all-atom MD simulations in a water-box to obtain equilibrated structures for further simulations, and to study the dynamics of the protein complex. The average contact map between JAK2-FERM-SH2$_{P37-T514}$ and PRLR-ICD$_{K235-E284}$ showed clusters of contacts in which residues from BOX1 of LID1 formed close contacts (avg. dist. ≤ 4Å) with residues from the F2 lobe (and the F1-F2 linker) and the SH2 domain of JAK2-FERM-SH2, respectively (***Figure 4 – figure supplement 1A***). C-terminally to BOX1, a second set of persistent contacts was observed, again involving charged and hydrophobic residues including F255, L259, E261, K262 and K264 from PRLR-ICD$_{K235-E284}$. Conservation analysis using ConSurf (Ashkenazy et al., 2016; Landau et al., 2005) (***Figure 4 – figure supplement 1B-D***) showed conserved residues in the interface, particularly those of BOX1 of PRLR (P245, P248, K251, I252) (***Figure 4 – figure supplement 1B),*** while a patch of conserved residues (T225, I229 and F236) in JAK2-FERM-SH2 formed close contact with residues from PRLR BOX1. JAK2 residues V183 and L184 interacted with the backbone of $_{251}$KIK$_{253}$ of PRLR-ICD, whereas other, less conserved residues such as E173 and E177 formed transient salt-bridges with K251 and K253 of PRLR-ICD (see ***Figure 4 – figure supplement 1A)***. The contact map also showed that the N-terminus of the ICJM remained flexible without close contacts with JAK2-FERM-SH2 (avg. dist. ≥ 6Å).

Next, an equilibrated structure of the JAK2-FERM-SH2:PRLR-ICD$_{K235-E284}$ complex was used to build a coarse-grained model, which was then placed near lipid bilayers of different lower leaflet composition. A number of randomly positioned starting orientations were placed ~7 Å below the lower leaflet (16 orientations for the POPC:POPS:PI(4,5)P_2 (80:10:10) membrane and eight for the POPC:POPS (70:30) membrane). In addition we included twelve orientations of JAK-FERM-SH2 without the PRLR-ICD$_{K235-E284}$ placed near a POPC:POPS:PI(4,5)P_2 (80:10:10) membrane. For the JAK2-FERM-SH2:PRLR-ICD$_{K235-E284}$ complex near a 70:30 POPC:POPS membrane, binding to the lower leaflet was observed for only three of the eight systems (***Figure 4 – figure supplement 2A***). In contrast, when PI(4,5)P_2 was present (10%), rapid binding of the complex to the membrane was observed in all simulations reaching 97% saturation (***Figure 4 – figure supplement 2A***). Both proteins in the complex showed specific clusters of residues with contacts to PI(4,5)P_2, POPS and POPC, independent of the initial orientations (***Figure 4BC***). The number of contacts formed was higher for the simulations with PI(4,5)P_2. This suggests that contacts with other components of the membrane occur close to the bound PI(4,5)P_2. Overall, the PRLR-ICD $_{K235-E284}$ showed a pattern of lipid contacts similar to the simulations of PRLR TMD-ICD$_{G204-H300}$ with the POPC:POPS:PI(4,5)P_2 (80:10:10) membrane (***Figure 4C***), with residues K$_{235}$GY$_{237}$contacting PI(4,5)P_2 headgroups for at least 50% of the total contact time and with insertion into the membrane; note that this occurs even though PRLR-ICD$_{K235-E284}$ is not tethered to the membrane via the TMD. Also, like in the PRLR TMD-ICD$_{G204-H300}$ simulations, contacts made by C242 and I243 to POPC were still present. In contrast, contacts by other residues from BOX1 and the KIK motif has lower populations. However, and as expected from the location of the most frequent PRLR-ICD $_{K235-E284}$/lipid contacts, JAK2-FERM-SH2 had more contacts in the F2 lobe of the FERM domain, mainly involving residues I223, L224, R226, K227 and R230, constituting the regions where the N-terminus of PRLR-ICD$_{K235-E284}$ is bound (***Figure 4B***). In the JAK2-FERM-SH2 simulations without PRLR-ICD and near a

POPC:POPS:PI(4,5)P_2 (80:80:10) membrane, we observed that simulations initiated in eleven out of the twelve orientations ended up binding to the membrane (***Figure 4 – figure supplement 2A***). In this case, the overall binding pattern of protein-lipid contacts remained similar.

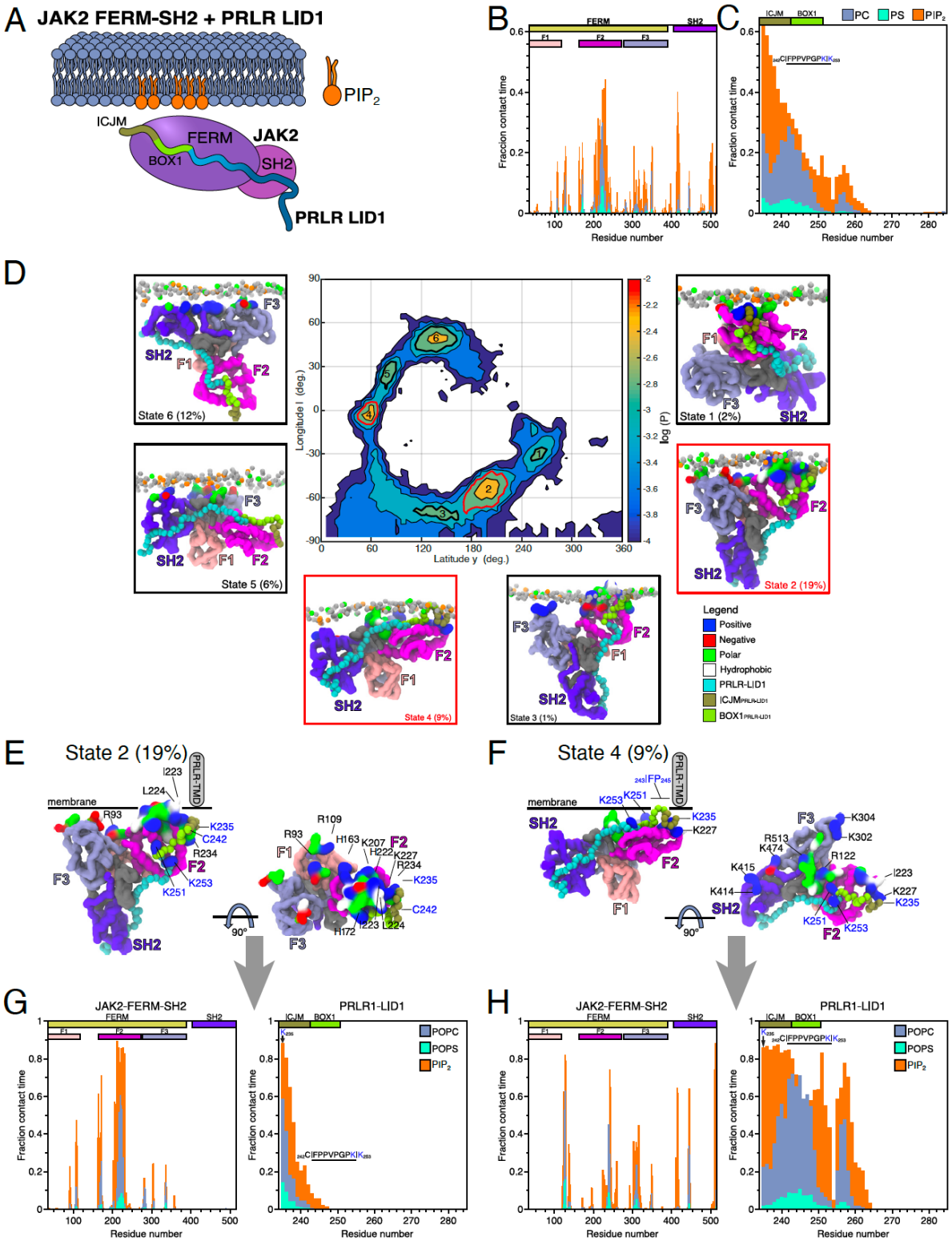

Fig. 4. Protein – lipid interactions of the JAK2-FERM-SH2 PRLR-ICD$_{LID1}$ complex obtained from CG-MD simulations. **A)** Schematic representation of the simulated system. Combined **B)** JAK2-FERM-SH2-lipid and **C)** PRLR-ICD$_{LID1}$-lipid contact frequency histograms for the 16 CG simulations of the JAK2-FERM-SH2 +PRLR-ICD$_{LID1}$+ POPC:POPS:PI(4,5)P_2 system. **D)** Distribution of the orientations adopted by the JAK2-FERM-SH2 + PRLR-ICD$_{LID1}$ complex when bound to lipids taken from the 16 simulations with POPC:POPS:PI(4,5)P_2 in the lower-leaflet. The snapshots surrounding the map correspond to representative conformations of the highlighted states also indicating the fraction total bound time for which each state was observed. Representative conformations of **E)** State 2 and **F)** State 4. The grey cylinder depicts the position where PRLR-TMD should be located. Representative protein-lipid contact histograms for **G)** State2 and **H)** State4 colored as in panels B and C.

Figure supplement 1: *Analysis of the JAK2-FERM-SH2- PRLR-ICD$_{LID1}$ AA-MD simulation***.**

Figure supplement 2. *Complementary analysis of Protein – lipid interactions of the JAK2-FERM-SH2 PRLR-ICD$_{LID1}$ complex obtained from CG-MD simulations*

Figure supplement 3. *Snapshots of the different binding states observed for the JAK2-FERM-SH2 – PRLR-ICD$_{LID1}$ complex with the complete structural model of JAK2*

In summary, our simulations showed that binding of JAK2 to the membrane was enhanced by the presence of PI(4,5)P_2 and that the ICD from PRLR and JAK2 formed a co-structure with PI(4,5)P_2 maintaining the contacts to the lipids observed for the individual proteins. The presence of PI(4,5)P_2 was essential for the membrane interactions.

The complex between JAK2-FERM-SH2 and LID1 shows preferential bound orientations with membranes containing PI(4,5)P_2

To characterize the membrane-bound modes of the complex in more detail, we took inspiration from Vogel *et al.* (Herzog et al., 2017) and constructed a map that represents the populations of different orientations of the JAK2-PRLR-ICD$_{K235-E284}$ complex relative to the membrane and extracted conformations to represent the most populated orientations as classified into states (***Figure 4D***). For the JAK2-PRLR-ICD$_{K235-E284}$ complex bound to the POPC:POPS:PI(4,5)P_2 (80:10:10) membrane, States 1–4 (~31% of the total contact time) showed the complex in an orientation where the N-terminus of PRLR-ICD$_{K235-E284}$ contacted and inserted into the bilayer similarly to what was observed in the PRLR TMD-ICD$_{G204-H300}$ simulations near a POPC:POPS:PI(4,5)P_2 bilayer. Of these four states, States 1, 2 and 3 had the F2 lobe of the JAK2-FERM domain and the ICJM region of PRLR-ICD$_{K235-E284}$ in contact with the membrane, penetrating below the headgroups, and acting as a pivot over which the protein-complex rotates, leaving the complex to hang as a "Y" from the membrane (See ***Figure 4DE*** and ***MOVIE1***). State 4 on the other hand, while retaining the main contact points, assumed a "flat" orientation with larger sections of the F2 lobe and F1-F2 linker from JAK2-FERM and the entire N-terminal half of PRLR-ICD$_{K235-E284}$ (residues K235-G263) making a substantial number of contacts with the membrane (***Figure 4DF*** and ***MOVIE2***). To examine whether the identified states are compatible with a functional state of the full-length kinase, we superimposed representative conformations of States 1 to 6 with that of the full-length JAK2 model obtained from the AlphaFold Protein Structure Database (UNIPROT O60674) (Jumper et al., 2021; Varadi et al., 2022). This procedure revealed that both the Y (States 1, 2 and 3), and Flat (State 4) states keep the other domains of JAK2 oriented towards the cytoplasmic space (***Figure 4 – figure supplement 3AD***), supporting that these states could be functionally relevant. Furthermore, in the context of JAK2 dimerization required for signalling (Ferrao et al., 2018), these states allow for the correct orientation

416 for kinase domain dimerization. The two remaining states (States 5 and 6) showed an inverted
417 orientation in which the main protein-lipid interactions were formed by residues from the F3 lobe of
418 FERM and the SH2 domain, bringing the F2 lobe and the ICJM region of the PRLR-ICD
419 unrealistically far away from the membrane and from the connecting end of the TMD. Thus, States 5
420 and 6 appear functionally irrelevant, as further demonstrated by the superposition of the full-length
421 AlphaFold model of JAK2 in which the kinase domains would clash with the bilayer (***Figure 4 –***
422 ***figure supplement 3EF***).
423
424 **Different membrane co-structures have different exposures relevant to signalling**
425 We analysed the protein-lipid interactions formed by States 2 (Y) and 4 (Flat) in more detail, and
426 despite overall similar contact profiles, some key differences were observed (***Figure 4E–4H***). For
427 the Flat state, an increase in contacts was seen for residues K235 to L260 of PRLR-ICD$_{K235-E284}$ with
428 a pattern similar to the one observed in the PRLR-TMD-ICD$_{G204-H300}$ simulations with PI(4,5)P_2
429 present. Dominant PI(4,5)P_2 contacts were seen for K235–C242, followed by POPC contacts for
430 residues C242–P248, with a second PI(4,5)P_2 contact peak for K251 and a third around H257. For
431 the Y state, only residues K235–Y237 made substantial contacts with PI(4,5)P_2 and/or POPC, leaving
432 BOX1 and the KIK motif exposed to the solvent and making contacts with JAK2. For JAK2-FERM-
433 SH2, the main difference between the Y and Flat states was a large decrease in contacts to the F2
434 lobe in the Flat state accompanied by an increase in contacts in F3 and SH2. Residues in the F2 lobe
435 involved in homodimerization, orientation and activation, including L224, K227, R230 and R234
436 (Wilmes et al., 2020) were only accessible in the Y state, and not in the Flat state. Thus, we speculate
437 that the Y and Flat states may mimic functionally relevant conformations pertaining to active and
438 inactive states of the signalling complex. Mapping of residues that make contacts with the bilayer in
439 the two states to the conservation maps shows that several positively charged residues of JAK2-
440 FERM-SH2 are largely conserved. Particularly K207, R226, K227 and R228 in F2 with high
441 population contacts with PI(4,5)P_2 in the Y state are highly conserved. Similar conservation was seen
442 for the positively charged residues K235, K414, K415 and R513, that form contacts with PI(4,5)P_2 in
443 the Flat state.
444
445 Similar simulations were performed near a POPC:POPS 70:30 bilayer, which resulted in only one of
446 eight systems showing stable binding to the bilayer characterized by only one state (***Figure 4 – figure***
447 ***supplement 2A,B***). Here, residues from the F2 lobe of JAK2 form contacts with POPS lipids in a
448 narrow peak containing residues Q219 to R230, while for PRLR-ICD $_{K235-E284}$, residues from the
449 ICJM (K235-C242) and the BOX1 region (C242-P248), make high frequency contacts with both
450 POPS and POPC (***Figure 4 – figure supplement 2DE***). Overall this state is somewhat similar to State
451 3 observed for the simulations with PI(4,5)P_2. Similarly, for our simulations of JAK2-FERM-SH2
452 without PRLR near a bilayer with PI(4,5)P_2, 11 out of 12 stable binding conformations revealed three
453 most populated states (E1, E2, E3) (***Figure 4 – figure supplement 2C***). Characterization of these in
454 terms of protein-lipid contact profiles revealed that the positively charged residues in the F2 lobe play
455 an important role in binding to PI(4,5)P_2 in a similar manner as observed for the Y and Flat states of
456 the complex (***Figure 4 – figure supplement 2F***). Indeed, States 2 and 3 (***Figure4 – figure supplement***

457 ***2GH***) show remarkable similarities with the Flat and Y state from the simulations of the JAK2-
458 FERM-SH2:PRLR-ICD$_{K235-E284}$ complex near a similar bilayer.
459
460 Overall, the simulations highlight preferential binding of both JAK2-FERM-SH2, both alone and in
461 complex with PRLR-ICD$_{K235-E284}$ to PI(4,5)P$_2$, and show that the absence of this lipid decreases the
462 level of LID1 binding to the bilayer. Even in the absence of TMD tethering, the most populated bound
463 states recapitulate the binding mode observed for the PRLR-ICD alone. Another key observation is
464 the existence of different states in which different regions of both JAK2 FERM-SH2 domain and
465 LID1 of PRLR are exposed to the solvent or hidden below the bilayer.
466
467 **Key residues for membrane interaction control cellular signalling efficiency**
468 From the NMR experiments and MD simulations we identified residues in LID1 that interact with
469 different components of the membrane and/or the FERM-SH2 domain of JAK2. This resulted in four
470 clusters positioned in the ICJM (K235-C242), the BOX1 region (C242–P248), two basic patches of
471 the KxK motif type (K251–K253 and K262–K264) and the region connecting them, respectively. To
472 decipher the specific role of these clusters for PI(4,5)P$_2$ interaction, we introduced four sets of
473 mutations in ICD$_{K235-G313}$ and investigated the effect on PI(4,5)P$_2$ interaction using NMR
474 spectroscopy. To avoid interfering directly with the BOX1 core motif (P245–P250) (Pezet et al.,
475 1997), only the short N-terminal CIF motif (C242–F244) was mutated to GAG (GAG mutant: C242G,
476 I243A, F244G), while the lysines in the KxK motifs (251–253 and 262–264) were all mutated to
477 either glycines (K4G mutant: K251G, K253G, K262G, K264G) or, for charge reversal, to glutamates
478 (K4E mutant: K251E, K253E, K262E, K264E). Finally, to investigate the role of hydrophobic
479 contacts in the region connecting the two KxK motifs, all four hydrophobic residues (I_{252}, F_{255}, L_{259}
480 and L_{260}) were mutated to glycines (φ4G mutant). ^{15}N-PRLR-ICD$_{K235-G313}$ and the four variants were
481 titrated with up to 25× molar excess of C$_8$-PI(4,5)P$_2$, keeping the concentration below the CMC. ^{1}H-
482 ^{15}N-HSQC spectra were recorded at each titration point and the changes in chemical shifts and signal
483 intensities were quantified (***Figure 5A***). Similarly to WT, all variants showed negligible chemical
484 shift changes (***Figure 5 – figure supplement 1***). Decreased peak intensities were observed for all
485 variants in the region of G236-D295, however, the changes were smallest for the φ4G mutant,
486 suggesting weaker affinities. Together, this indicates that the KxK motifs, the CIF-motif and the
487 hydrophobic residues are involved in PI(4,5)P$_2$ interaction, yet none of these residues are essential for
488 binding.
489
490 We observed dramatic increases in peak intensities for the K4G and φ4G variants in the presence of
491 5× and 10× molar excess of C$_8$-PI(4,5)P$_2$ when compared to WT (***Figure 5A***), suggesting chages in
492 the dynamics of the chain. To adress this, we probed the backbone dynamics by acquiring ^{15}N R_2
493 relaxation rates of the WT, K4G and φ4G variants in the absence of C$_8$-PI(4,5)P$_2$ (***Figure 5 – figure***
494 ***supplement 2***). Compared to the WT, no major changes in R_2 were observed for two variants. The
495 intensity increase observed for the K4G and φ4G variants during the titration with C$_8$-PI(4,5)P$_2$
496 therefore indicates increased backbone dynamics upon binding to C$_8$-PI(4,5)P$_2$ compared to the WT.
497 Although we cannot explain this observation, it suggests that binding to C$_8$-PI(4,5)P$_2$ increases the

dynamics of the first parts of the chain and thus require higher concentration of C_8-PI(4,5)P_2 to fully form the complex, as expected by the lower apparent affinity.

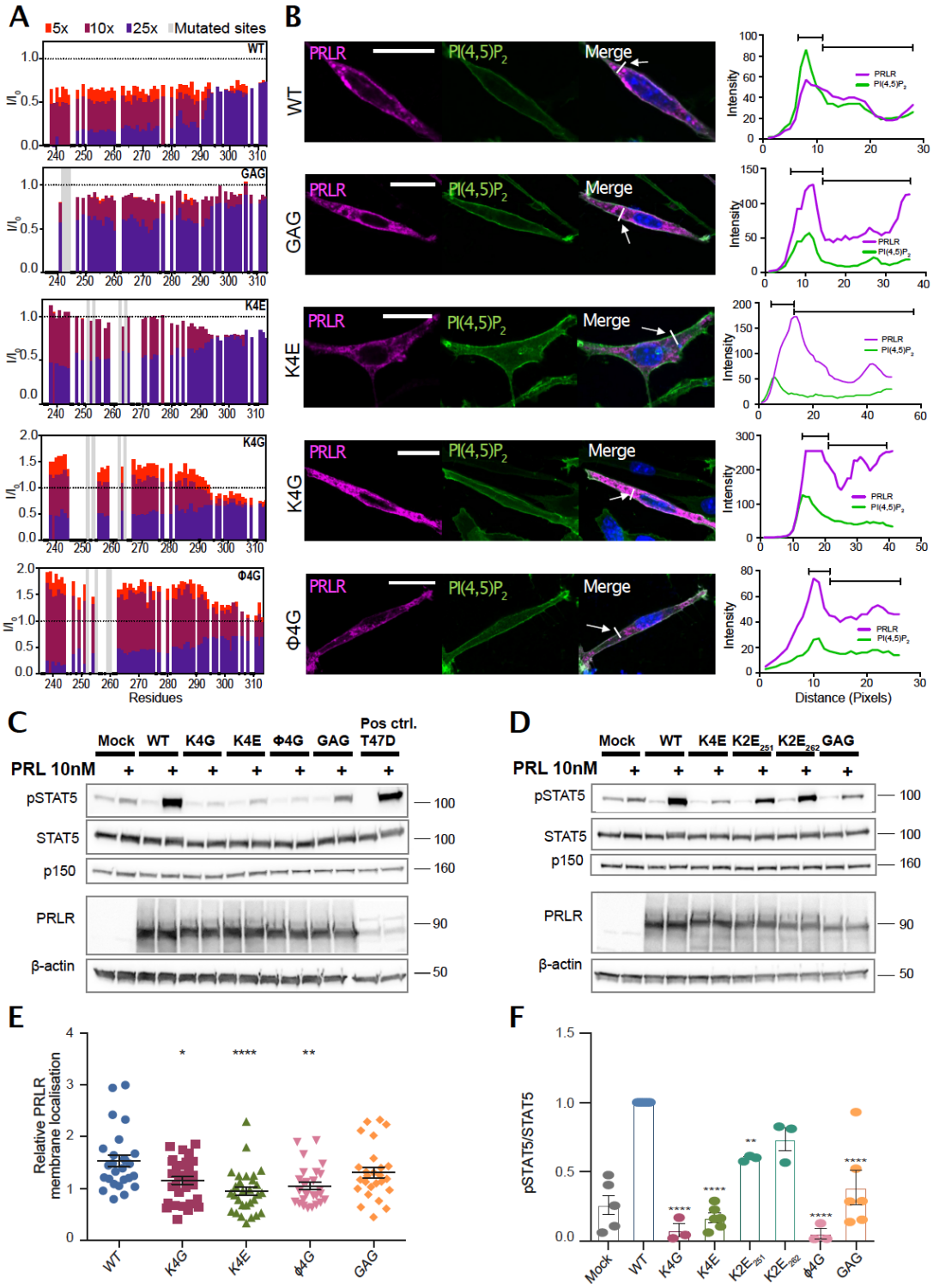

Fig. 5. PRLR variants with mutations in lipid interacting residues exhibit decreased PRL-stimulated STAT5 activation in AP1-2PH-PLCδ-GFP cells. A) NMR intensity changes of $ICD_{K235-G313}$ WT, K4G, K4E, φ4G and GAG variants upon titration with 5x, 10x and 25x molar excess C_8-PI(4,5)P_2 plotted against residue number. **B)** The PRLR variants (WT, K4G, K4E, φ4G, 3GAG) were transiently transfected in AP1 cells stably expressing the 2PH-PLCδ-GFP construct which visualizes the plasma membrane by binding PI(4,5)P_2. The cells were subsequently analysed by

immunofluorescence microscopy, using antibodies against PRLR (magenta) and GFP (green), as well as DAPI (blue) to mark nuclei. To the right, examples of an average line-scan for each PRLR variant is shown. The fluorescence intensity depicted along the white line drawn (arrow) and green fluorescence (plasma membrane) was used to divide the line in a plasma membrane section and intracellular section, and relative membrane localization was calculated as the average fluorescence of PRLR in the membrane section divided by that in the intracellular section. **C, D)** AP1-2PH-PLCδ-GFP cells were transiently transfected with PRLR variants (WT, K4G, K4E, φ4G, 3GAG, $K2E_{253}$, $K2E_{261}$) and incubated overnight followed by serum starvation for 16-17 h and were subsequently incubated with or without 10 nM prolactin for 30 min. The resulting lysates were analysed by western blot for STAT5, pSTAT5 (Y964), PRLR, β-actin and p150 levels. The immunoblots are representative of three biological replicates. **E**) Ratio of plasma membrane localized receptor compared to intracellular receptor, analysed by line-scans as in B. Each point represents an individual cell, and data are based on three independent biological experiments per condition. Graphs show means with SEM error bars. *P<0.05, **P<0.01 and ****P<0.0001. One-way ANOVA compared to WT, unpaired**. F)** Quantification of western blot results shown as pSTAT5 normalized to total STAT5, relative to the WT condition. Graphs show means with SEM error bars. *P<0.05 and **P<0.01. One-way ANOVA compared to WT, unpaired.

Source file 1: Raw western blots (relating to *figure 5C*)

Source file 2: Raw western blot (relating to *figure 5D*)

Source file 3: Data summaries (relating to *figure 5E,F*)

Figure supplement 1: *Chemical shift perturbations of $ICD_{K235-G313}$ of A) WT, B) K4E, C) GAG, D) K4G and E) ϕ4G variants.*

Figure supplement 2: *^{15}N R_2 relaxation rates of $ICD_{K235-G313}$ of WT (grey bars), K4G (blue dots) and ϕ4G (red squares) variants.*

To address the implications of $PI(4,5)P_2$ interaction for PRLR membrane localization and downstream signalling, and to separate the effect of perturbed membrane localization from actual $PI(4,5)P_2$ binding, we introduced the same four sets of mutations into the full-length PRLR. Together with WT PRLR, these were transiently transfected into AP1 mammalian epithelial cells, which were stably transfected with the fluorescent $PI(4,5)P_2$ reporter 2PH-PLCδ-GFP. The cells were subjected to fluorescence microscopy analysis of PRLR and the $PI(4,5)P_2$ reporter (Fig. 5B) and to western blot analysis of STAT5-activating phosphorylation (***Figures 5C-D, F-G***). None of the mutations fully abolished PRLR membrane localization. Western blot analysis showed that the protein expression levels were similar for WT PRLR and all PRLR variants (***Figure 5C***). However, compared to WT, the K4G, K4E and φ4G variants exhibited a significant reduction in membrane localization as determined by line scan analysis (***Figures 5B,E***). The PRL-induced STAT5 activation was significantly decreased in cells expressing either the K4G, K4E or the φ4G variants, whereas STAT5 activation in cells expressing the GAG variant was not significantly different from that of WT expressing cells (***Figures 5C,F***). Decomposing the K4E variant into two individual mutants, in which only one of the two KxK motifs was changed ($K2E_{251}$ and $K2E_{262}$) showed that the reduction in STAT5 activation was attenuated in the variants with the individual mutations, compared to the drastic decrease observed for the K4E mutant (***Figure 5D,G***). Thus, both KxK motifs are important for JAK/STAT activation.

Taken together, these results show that while our data are consistent with the decreased membrane localization contributing to the reduction of STAT5 activation, it is unlikely to account fully for the effect observed for the K4G, K4E or the φ4G variants. This indicates that the cellular effects arise from a combined effect on $PI(4,5)P_2$- and JAK2 interactions. The MD simulations indicated that only

551 the first KxK motif is involved in lipid interaction while the second KxK motif is involved in JAK2
552 interaction. Thus, the reduction in JAK/STAT activation in these variants likely arises from a
553 combined effect of abolishing both PI(4,5)P_2- and JAK2 interaction within the LID1 region, which
554 support the suggestion that co-structure formation between JAK2, PRLR and the membrane is critical
555 for optimal JAK/STAT signalling.
556
557 **Discussion**
558 The sequence of the human PRLR has been known for more than 35 years (Boutin et al., 1988). Little
559 attention has, however, been given to the role of membrane composition for PRLR signalling, despite
560 it being placed in the plasma membrane where phosphoinositide levels are highly dynamic and
561 spatially variable, and being linked to cancer with lipid deregulation (Dadhich and Kapoor, 2022).
562 Here we asked if JAK2 and PRLR-ICD share a PI(4,5)P_2 binding site and if and how the binding to
563 PI(4,5)P_2 plays a role in the orientation of these proteins with respect to the membrane. Integrating
564 MD simulations with biophysical and cellular experiments has been critical in this endeavor. Our first
565 goal was to identify the residues of LID1 involved, as well as the structure formed—if any—in the
566 protein–lipid complex. Our results suggest that the residues that form the ICJM and BOX1 regions
567 of the ICD interact with the lipids via non-specific hydrophobic interactions that involve penetration
568 of the bilayer below the headgroups. This in turn enables positively charged residues of the $_{251}$KIK$_{253}$
569 motif to stablish ionic interactions with PI(4,5)P_2 and in doing so the region folds into an extended
570 structure, similar to structures of other cytokine receptors in complex with either JAK1 or TYK2
571 (Wallweber et al., 2014; Zhang et al., 2016). In turn, PI(4,5)P_2 lipids accumulate around the TMD
572 and LID1 of PRLR, suggesting a relevant functional role of the interaction.
573
574 The results highlight the capacity of the LID1 to establish highly populated and specific interactions
575 with PI(4,5)P_2 via residues essential for its interaction with JAK2. Therefore, we addressed whether
576 LID1 in complex with the FERM-SH2 domain of JAK2 could engage with the lipid bilayer in the
577 absence of the TMD and with or without PI(4,5)P_2 lipids. Indeed, PI(4,5)P_2 was required for binding
578 of the complex to the membrane, as the presence of only POPS in the lower leaflet was not enough
579 to sustain binding despite its negative charge. Remarkably, when PI(4,5)P_2 was present, we observed
580 specific binding orientations that positioned the ICJM region of the LID1 in the same position as
581 when tethered to the TMD. Furthermore, in the complex, the protein-lipid contact profiles were
582 similar to the one observed for LID1 alone suggesting the PI(4,5)P_2 binding pattern to be maintained
583 in complex with JAK2. A detailed study of two of the most populated PRLR-bound states of JAK2
584 revealed a striking difference in orientation and contact pattern with the lipids, that could shed light
585 on functionally relevant states. For example, the most populated state, the Y state, had contacts from
586 the F2 lobe of the JAK2-FERM-SH2 domain and the ICJM of the PRLR, which penetrated the
587 membrane forming hydrophobic interactions with the acyl chains. In this orientation, regions of both
588 JAK2 and the PRLR that have been associated with receptor dimerization and activation for signaling
589 (Ferrao et al., 2018; Wilmes et al., 2020) are exposed to solvent and available for interactions. For
590 the Flat state, we observed a drastic change in the protein-lipid contact profiles for both proteins, but
591 more markedly for LID1. While the main interaction site remains the F2 lobe of JAK2 and the ICJM
592 of the PRLR, the N-terminal residues of the LID1 now lie sandwiched between the membrane and

JAK2-FERM-SH2 domain and recapitulates the binding pattern observed from TMD-ICD$_{F206-H300}$ simulations with membranes containing PI(4,5)P_2. Remarkably, in this Flat state, most of the accessible region in the Y states is now hidden in the membrane. Thus, we speculate that the Y and Flat states mimic an available and hidden state, respectively, that could be relevant for regulation of dimerization and activation of signaling. Interestingly, one residue that has been suggested to play a major role in JAK2 membrane association, orientation, dimerization, and activation is L224 (Wilmes et al., 2020). This residue anchors into the membrane only in the Y-state, and not in the Flat-state. Similarly, in simulations where L224 was mutated to glutamate, a change in preferred orientation together with loss of dimerization and JAK2 and STAT5 phosphorylation was observed (Wilmes et al., 2020). This further highlight that the orientation of the PRLR-JAK2 complex relative to the membrane has functional relevance. Importantly, the presence of PI(4,5)P_2 in the membrane structurally tightens the path from the ECD, folding the ICJM and BOX1 in an extended structure, making transmission of information of hormone binding possible. Thus, signal relay by disordered linker of the PRLR can now be possible through its complex formation with the membrane and JAK2 (***Figure 6***).

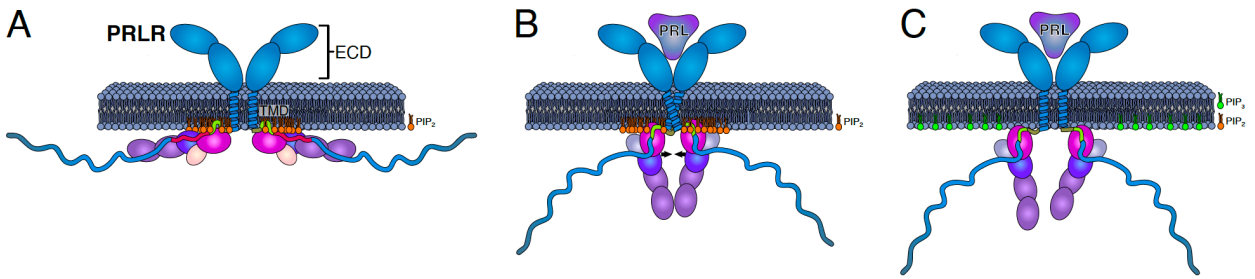

Fig. 6. Model of how co-structure formation between JAK2, PRLR and PI4(4,5)P_2 may contribute to signalling fidelity. The suggested states in signalling would be **A**) the inactive state of the co-structure exemplified by the Flat orientation. **B**) The hormone bound state expemplfied by the co-structure in the Y orientation. **C**) Phosphorylation of PIP(4,5)P_2 to PI(3,4,5)P_3 for which the PRLR has no affinity may lead to downregulation and/or termination of signalling. The colour scheme of the proteins is identical to Fig.4.

Lastly, we tested the functional relevance of our observations by mutating residues that appeared significant for PI(4,5)P_2:PRLR:JAK2 co-structure formation and determining their impact on cellular PRL signaling. Both KxK motifs and the hydrophobic residues connecting them were important for PI(4,5)P_2 interaction, PRLR membrane localization and cellular JAK2/STAT5 signaling. From the MD simulation it was however evident that not all residues in these motifs were in direct contact with the membrane, further highlighting that co-structure formation between PRLR, JAK2 and the membrane is essential for optimal signal transduction. Another interesting observation was that even though mutating the CIF motif had the largest impact on PI(4,5)P_2 binding, it had only a limited effect on cellular JAK2/STAT5 signaling. Since the NMR results suggested that the ICJM serves as a primary PI(4,5)P2 anchoring point facilitating additional contact along the chain, this could indicate that a cooperative interaction within the co-structure is needed to control signaling and that PI(4,5)P_2 interaction is necessary for proper and substantial co-structure formation.

629 The PI(4,5)P_2-specific interactions observed point toward a possible regulatory role of PI(4,5)P_2 in
630 PRLR signaling. Our simulations showed that the membrane embedded TMD-ICD$_{F206-H300}$ was
631 associated with an accumulation of PI(4,5)P_2 around the TMD. One of the suggested roles of
632 PI(4,5)P_2 as a regulatory lipid is indeed to form microdomains around proteins and reduce their lateral
633 movement (Trimble and Grinstein, 2015; van den Bogaart et al., 2011). Another possible role can be
634 inferred from previous studies on the EGFR, signaling throught which is inhibited by PI(4,5)P_2.
635 Evidence suggests a positive feedback loop where inhibition is released upon activation, because
636 PI(4,5)P_2 is hydrolyzed to DAG and IP_3 by PLC_y (Maeda et al., 2018; McLaughlin et al., 2005).
637 Specifically, we have previously shown that PRLR does not interact with PI(3,4,5)P_3 (Haxholm et
638 al., 2015). As PI(4,5)P_2 is phosphorylated by the PI3-kinase to PI(3,4,5)P_3 during PRLR signaling
639 (Aksamitiene et al., 2011; Yamauchi et al., 1998), this could indicate a way of attenuating signaling.
640 Whether hydrolysis of PI(4,5)P_2 by PLC_y is relevant for PRLR signaling is not known.
641
642 **Conclusions**
643 Signal transduction by single-pass receptors through the membrane is still an enigma. In the present
644 work we identify co-structure formation of the disordered LID1 of the PRLR, the membrane
645 constituent PI(4,5)P_2 and the FERM-SH2 domain of the JAK2, and demonstrate its importance for
646 PRLR signalling. This co-structure has at least two orientations, a Y-shaped state extending from the
647 membrane and a Flat-state with sites hidden in the membrane. The co-structure led to accumulation
648 of PI(4,5)P_2 at the TMD interface and mutation of residues identified to specifically interact with
649 PI(4,5)P_2 negatively affected PRL-induced STAT5 activation. Facilitated by the co-structure, the
650 disordered ICJM folds into an extended structure, tightening the path from the ECD to the ICD. We
651 suggest that the co-structure formed between receptor, kinase and PI(4,5)P_2 is critical for signal relay
652 from the extracellular to the intracellular side of the membrane, and that different orientations of the
653 co-structure exist that may represent inactive and active states.
654
655 **Materials and Methods**
656 **Expression and purification of TMD $_{F206-V240}$, TMD-ICD $_{F206-S270}$ and ICD$_{G236-Q396}$**
657 PRLR-ICD$_{G236-Q396}$ was produced as described in (Haxholm et al., 2015), and TMD$_{F206-V240}$ and
658 TMD-ICD$_{F206-S270}$ were produced as described in (Bugge et al., 2015).
659
660 **Expression and purification of ICD$_{K235-G313}$ and variants (K4E, K4G, ϕ4G and GAG)**
661 ICD$_{K235-G313}$ and variants hereof, K4E (K251E, K253E, K262E, K264E), K4G (K251G, K253G,
662 K262G, K264G), ϕ4G (I252G; F255G, L259G, L260G) and GAG (C242G, I243A, F244G) were all
663 produced as follows: Competent BL21(DE3) were transformed using heat shock transformation with
664 pET24a+ plasmids encoding the protein of interest with N-terminal His_6-SUMO tag. One colony
665 was used to inoculate 10 mL of LB media with 50 µg/mL Kanamycin and incubated overnight at 37
666 °C at 160 RPM. The overnight culture was used to inoculate 1L M9 minimal media (3 g/l KH_2PO_4,
667 7.5 g/l Na_2HPO_4, 5 g/l NaCl, 1 mM $MgSO_4$, 4 g/l glucose, 1 g $^{15}NH_4Cl_2$, 1ml M2 trace solution, 50
668 µg/mL Kanamycin) and grown at 37 °C. At OD600 ~0.6 recombinant protein expression was induced
669 with 0.1 mM IPTG for 4H at 37 °C. Cells were harvested by centrifugation (5000xg, 20 min, 4°C)
670 and kept at -20 °C until purification. Cells were resuspended in 35 mL Buffer A (10 mM imidazole,

671 50 mM Tris (pH 8), 150 mM NaCl, 2 mM dithiothreitol (DTT) and lysed with French press at 25
672 kpsi, followed by centrifugation at 20.000xg, 45 min, 4 °C. The supernatant was applied to 5 mL of
673 pre-equilibrated Ni-NTA beads and incubated for 15 min followed by 50 mL wash with Buffer B 10
674 mM Imidazole, 50 mM Tris (pH 8), 1M NaCl, 2mM DTT) and 50 mL wash with Buffer A. Protein
675 was eluted with 10 mL Buffer C (250 mM Imidazole, 50 mM Tris (pH 8), 150 mM NaCl, 2 mM
676 DTT). The elution was supplemented with 0.01 mg ULP-1 and dialysed against 1 L of dialysis buffer
677 (50 mM Tris (pH 8), 150 mM NaCl, 1 mM DTT) overnight at 4 °C. The sample was re-applied to the
678 Ni-NTA column and incubated for 15 min. Flow through containing cleaved protein was collected,
679 and the remaining protein was eluted with 10 mL Buffer C. The sample was supplemented with 10
680 mM DTT before heating at 75 °C for 5 min with gentle rotation of the sample throughout. Sample
681 was transferred directly to ice for 10-15 min incubation followed by centrifugation at 20.000xg, 10
682 min, 4 °C. The supernatant was concentrated and supplemented with 5 mM betamercaptoenthaonl
683 (b-ME) before application to a HiLoad 16/60 Superdex75 prep grade column equilibrated in 20 mM
684 Na_2HPO_4/NaH_2PO_4, 150 mM NaCl, 5 mM b-ME (pH 7.3). Fractions containing pure protein were
685 pooled and concentrated
686
687 **CD spectroscopy**
688 The peptides covering residues K235-D256 (Pep1) and K253-T280 (Pep2), respectively were
689 purchased from KJ Ross (DK) at 95% purity from HPLC purification. The peptides were dissolved
690 in 10 mM Na_2HPO4/Na_2HPO4, pH 7.3 to a final concentration of 40 µM (Pep1) and 25 µM (Pep2)
691 and titrated with TFE or C_8-PI(4,5)P_2. The spectra were recorded in a 1mm Quartz cuvette on a Jasco-
692 810 spectropolarimeter purged with 8 l/min N_2 at 25 °C. A total of 10 accumulations were acquired
693 from 260-190 nm with the following settings: 0.5 nm data pitch, 1 nm band width, response time of
694 2 seconds, scanning speed of 10 nm/min. A background reference was recorded at identical settings
695 for each sample and subtracted from the relevant spectrum. The spectra were processed by fast
696 Fourier transform filtering and ellipticity converted to mean residual ellipticity ($[\theta]_{MRW}$)
697
698 **NMR spectroscopy**
699 *TMD* $_{F206\text{-}V240}$ *and TMD-ICD* $_{F206\text{-}S270}$
700 ^{15}N-labelled or ^{13}C,^{15}N-labeled TMD-ICD$_{F206\text{-}S270}$ was solubilized in molar excess 1,2-dihexanoyl-
701 sn-glycero-3-phosphocholine (DHPC) dissolved in 50 mM NaCl, 20 mM Na_2HPO_4/NaH_2PO4 buffer,
702 pH 7.2. Subsequently, the DHPC embedded TMD-ICD$_{F206\text{-}S270}$ was subjected to thorough buffer
703 exchange in a 3 kDa cutoff spinfilter to remove residuals. For reconstitution into POPC SUVs, ^{15}N-
704 labeled TMD-ICD$_{F206\text{-}S270}$ was solubilized in 300 µL 5:1 methanol:chloroform and mixed with molar
705 excess POPC dissolved in chloroform. The constituents were mixed, followed by evaporation of the
706 organic solvent under a stream of N_2. When the lipid film appeared dry, it was either left under a
707 stream of N_2 or placed under vacuum for at least an hour. The resulting proteoliposome film was
708 rehydrated with 1 mL of 50 mM NaCl, 20 mM Na_2HPO_4/NaH_2PO_4 buffer, pH 7.2, followed by
709 extensive dialysis against the buffer in a 3.5 kDa MWCO dialysis tube at 4 °C. Subsequently, the
710 proteoliposome solution was sonicated in an ultrasonication bath or, if the solution did not clarify,

711 with an UP400S Ultrasonic Processor, in rounds of 2 s with 30 s rest between runs. Finally, the sample
712 was concentrated in a 3 kDa cutoff spinfilter.
713 All NMR samples of ^{15}N-labelled or ^{13}C,^{15}N-labelled TMD-ICD$_{F206-S270}$ were added 10% (v/v)
714 D_2O, 2 mM tris(2-carboxyethyl)phosphine (TCEP), 1 mM sodium trimethylsilylpropanesulfonate
715 (DSS), 0.05% (v/v) NaN_3, and 50 mM NaCl, 20 mM Na_2HPO_4/NaH_2PO4 buffer (pH 7.2) to a final
716 volume of 370 µL followed by pH-adjustment to 7.2 (if needed). All spectra were acquired at 37 °C
717 because the peak intensities of the TMD region decreased at lower temperatures. Free induction
718 decays were transformed and visualized in NMRPipe (F Delaglio et al., 1995) and analysed using the
719 CcpNmr Analysis software (Vranken et al., 2005). Proton chemical shifts were referenced internally
720 to DSS at 0.00 ppm, with heteronuclei referenced by relative gyromagnetic ratios. For assignments
721 of backbone nuclei, heteronuclear NMR spectra of a sample containing 0.5 mM ^{13}C,^{15}N-labelled
722 TMD-ICD$_{F206-S270}$ in 500 times molar excess DHPC were acquired on a Bruker 750-MHz (^{1}H)
723 equipped with a cryoprobe. HNCACB and CBCA(CO)NH spectra were acquired with 32 and 40 of
724 transients, respectively, and 20% non-uniform sampling (Mayzel et al., 2014), and used for manual
725 backbone assignments. SCSs were calculated using random coil chemical shifts from (Kjaergaard et
726 al., 2011) (obtained by supplying primary structure, pH and temperature to the webtool
727 http://www1.bio.ku.dk/english/research/bms/research/sbinlab/groups/mak/randomcoil/script/),
728 which were subtracted from the assigned TMD-ICD $_{F206-S270}$ chemical shifts.
729 The ^{1}H,^{15}N-HSQC spectrum of 0.4 mM ^{15}N-labelled TMD-ICD$_{F206-S270}$ in POPC SUVs (100 times
730 molar excess of POPC) was acquired on a Varian INOVA 750- MHz (^{1}H) spectrometer equipped
731 with a room temperature probe. The number of transients was 104.
732
733 *ICD$_{K235-G313}$*
734 ICD$_{K235-G313}$ and the four variants (K4E, K4G, phi4G and GAG) were dialyzed at 4 °C overnight
735 against 20 mM Na_2HPO_4/NaH_2PO_4 (pH 7.3), 150 mM NaCl. The samples of 50 µM protein were
736 added 1 mM TCEP, 0.25 mM DSS and 10% (v/v) D_2O and centrifuged at 20.000 xg, 4 °C for 10 min
737 and transferred to 5mm Shigemi BMS-3 tubes. All NMR experiments were recorded at 5 °C on a
738 Bruker Avance III 600 MHz (^{1}H) spectrometer equipped with cryogenic probe. Free induction decays
739 were transformed and processed in qMDD (Orekhov and Jaravine, 2011), phased in NMRDraw
740 (Frank Delaglio et al., 1995) and analysed in CcpNMR analysis software (Vranken et al., 2005).
741 Proton chemical shifts were referenced to DSS and nitrogen and carbon to their relative gyromagnetic
742 ratios. ^{1}H-^{15}N-HSQC experiments were acquired using non-uniform sampling (Mayzel et al., 2014)
743 and recorded on 50 µM ^{15}N-ICD$_{K235-G313}$ (or variants) in the absence and presence of 5x, 10x and 25x
744 molar excess of C_8-PI(4,5)P_2 (Avanti Lipids 850185).
745 Transverse ^{15}N relaxation rates (R_2) of ICD$_{K235-G313}$ and the two variants, K4G and φ4G, were
746 acquired on Bruker Avance III 600 MHz (^{1}H) spectrometer with varying relaxation delays of 0 ms,
747 33.92 ms, 67.84 ms, 135.68 ms, 169.6 ms, 203.52 ms, 271.36 ms and 339,2 ms, measured in triplicates
748 and peak intensities fitted to single-exponential decays.
749
750 **Cell lines and media**
751 AP1-2PH-PLCδ-GFP cells (From J. Snipper; vector from Addgene plasmid #35142) were grown in
752 Minimum Essential Medium Eagle (EMEM, Gibco) containing 10% Fetal Bovine Serum (Sigma

753 Aldrich), 1% penicillin/streptomycin (Sigma), and 1% L-glutamine (Sigma). Stable AP1 clones
754 expressing 2PH-PLCδ-GFP were grown in the same medium, containing 600 µg/mL geneticin
755 (Merck-Millipore) to maintain expression of 2PH-PLCδ-GFP. Cell lines were maintained at 37 °C
756 with 95% humidity and 5% CO_2 and were passaged by gentle trypsination for a maximum of 15
757 passages.
758
759 **Immunoblotting**
760 Cells were grown to ~80% confluence in 6-well plates, washed in ice-cold PBS, lysed in boiling lysis
761 buffer (1% SDS, 10 mM Tris–HCl, pH 7.5, with phosphatase inhibitors), boiled for 1 min, sonicated,
762 and centrifuged to clear debris. Identical amounts of protein (12 µg/well) diluted in NuPAGE LDS
763 sample buffer (Novex) with 50% 0.5M DTT were boiled for 5 min, separated on Bio-Rad 10% Tris-
764 Glycine gels, and transferred to nitrocellulose membranes using the Trans-Blot Turbo Transfer
765 system (Bio-Rad). Membranes were stained with Ponceau S to confirm equal loading, blocked for 1
766 h at 37 °C in blocking buffer (TBST, 5% nonfat dry milk), and incubated with the relevant primary
767 antibodies in blocking buffer overnight at 4°C. After washing in TBST (TBS + 0.1% Tween-20),
768 membranes were incubated with HRP-conjugated secondary antibodies (1:2000, Sigma), washed in
769 TBST, and visualized using ECL reagent (Bio-Rad). Protein bands were quantified by densitometry
770 using ImageJ software, and normalized to those of STAT5 and then to WT.
771
772 **Immunofluorescence analysis**
773 For immunofluorescence experiments, cells were grown on 12 mm round glass coverslips to ~80%
774 confluency and fixed in 2% PFA (30 min at RT). Coverslips were washed three times for 3 x 5 min
775 in PBS, permeabilized for 15 min (0.5% Triton X-100 in TBS), blocked for 30 min (5% BSA in
776 TBST), and incubated with primary antibody in TBST + 1% BSA at RT for 1.5 h. Coverslips were
777 again washed in TBST + 1% BSA, and incubated with AlexaFluor488 and AlexaFluor568 conjugated
778 secondary antibody (1:600 in TBS + 1% BSA) for 1.5 h. Finally, coverslips were incubated with
779 DAPI (1:1000) for 5 min to stain nuclei, washed in TBST, and mounted in N-propyl-gallate mounting
780 medium (2% w/v in PBS/glycerol). Cells were visualized using the Olympus IX83 microscope with
781 a Yokogawa spinning disc confocal unit, using a 60X/1.4 NA oil emersion objective. Image
782 adjustments were carried out using ImageJ software. Line scans were performed using the
783 ColorProfiler ImageJ software plugin.
784
785 **Primary antibodies**
786 PRLR (Santa Cruz #SC20992), STAT5 (Santa Cruz #SC835), pSTAT5 (Y964) (Cell Signaling
787 #CS4322), p150 (BD #BD610473), β-actin (Sigma Aldrich #A5441).
788
789 **Modelling of simulated proteins**
790 *PRLR TMD-LID1 on a lipid bilayer*
791 To build a model of the hPRLR-TMD-ICD-LID1region (G204 to H300) we used the MODELLER
792 interface of Chimera (Pettersen et al., 2004; Webb and Sali, 2016). The structure of hPRLR-TMD
793 (PDB 2N7I (Bugge et al., 2016)) was used as template for the transmembrane helix (in this structure
794 the residue at position 204 (P) was mutated to a G thus, in our model position 204 corresponds to a

795 glycine) and due to the lack of structural templates for the ICD, it was modelled as a disordered coil.
796 This all-atom model was used to build coarse-grained simulation systems where the TMD was
797 embedded in different lipid bilayers composed of POPC in the upper leaflet and either: i) POPC:POPS
798 (70:30), ii) POPC:POPS:PI(4,5)P_2 (90:5:5) and iii) POPC:POPS:PI(4,5)P_2 (80:10:10) in the lower
799 leaflet using the CHARMM-GUI martini_maker module (Jo et al., 2008; Qi et al., 2015). The
800 resulting systems were built using the Martini 2.2 forcefield topology and were later adapted to the
801 Martini 3 (version m3.b3.2) (Souza and Marrink, 2020) topology using the martinize2.py tool.
802 Secondary structure restraints from the Martini forcefield were only applied to the TMD and no
803 harmonic bond restraints were defined in the building of these systems.
804
805 *All-atom models of JAK2-FERM-SH2 and its complex with PRLR-ICD$_{LID1}$*
806 To build the JAK2-FERM-SH2 + PRLR-ICD$_{K235-E284}$ complex the following structures where used:
807 JAK1-FERM-SH2 + IFNLR1 (PDB 5L04 (Zhang et al., 2016)), TYK2-FERM-SH2 + IFNAR1 (PDB
808 4PO6 (Wallweber et al., 2014)) and JAK2-FERM-SH2 (PDB 4Z32 (McNally et al., 2016)). A
809 structural alignment of the three FEMR-SH2 domains was performed with STAMP (Russell and
810 Barton, 1992) using the Multiseq module (Roberts et al., 2006) of VMD (Humphrey et al., 1996).
811 The model of PRLR-ICD$_{K235-E284}$ was generated with the MODELLER interface of Chimera using as
812 template the aligned receptor-ICD regions present on the structures 5L04 and 4PO6. A total 200
813 models were generated, and the best in terms of its DOPE score (Shen and Sali, 2006) was selected
814 for further use. This resulted in a model of PRLR-ICD$_{K235-E284}$ bound to JAK2-FEMR-SH2. By
815 combining this model with chain A of PDB 4Z32, a structural model of the JAK2-FERM-SH2 +
816 PRLR-ICD$_{K235-E284}$ complex was obtained. All-atom simulation systems were built for JAK2-FERM-
817 SH2 and the JAK2-FERM-SH2+PRLR-ICD$_{K235-E284}$ complex model. The missing residues on the
818 loop of F3 of JAK2-FERM-SH2 were completed using CHARMM-GUI pbd-reader module (Jo et
819 al., 2014, 2008). Hydrogen atoms were automatically added to the protein using the psfgen plugin of
820 VMD (Humphrey et al., 1996). Aspartate, glutamate, lysine, and arginine residues were charged, and
821 histidine residues were neutral. Simulation boxes comprised of solvent and 150 mM NaCl were
822 generated using the CHARMM-GUI solution-builder module (Jo et al., 2008; Lee et al., 2016) using
823 CHARMM36m (Huang et al., 2017) parameters and topologies for the protein and the TIP3P water
824 model for the solvent.
825
826 *Coarsed-grained models of JAK2-FERM-SH2 and its complex with PRLR-ICD$_{LID1}$*
827 To build coarse-grained models of JAK2-FERM-SH2 and complex between JAK2-FERM-SH2 and
828 PRLR-ICD$_{K235-E284}$ complex, a conformation from their respective all-atom MD simulations of the
829 complex was taken after 150 ns (see below). These conformations were used to generate a CG model
830 using the martinize.py script. The Martini 2.2 forcefield (de Jong et al., 2013) was used and
831 intramolecular elastic bonds were defined for JAK2-FERM-SH2 in both systems. To keep the
832 complex formed and to avoid a "collapse" of the disordered PRLR-ICD$_{LID1}$, inter-molecular harmonic
833 bonds were also defined between JAK-FERM-SH2 and PRLR-ICD$_{K235-E284}$ in the complex. In both
834 cases, a force constant of 400 kJ mol^{-1} nm^{-2} and lower and upper elastic bond cut-offs of 5Å and 9Å,
835 respectively were used.
836

Coarse-grained models of JAK2-FERM-SH2 and JAK2-FERM-SH2 + PRLR-ICD$_{LID1}$ near a lipid bilayer

The relaxed CG-model of the JAK2-FERM-SH2 + PRLR-ICD$_{LID1}$ complex or JAK2-FERM-SH2 alone (see below) was placed near (~ 7Å) pre-equilibrated lipid bilayers with wo different compositions: POPC on the upper leaflet and two differen compositions on the lower leaflet: i) POPC:POPS (70:30), and ii) POPC:POPS:PI(4,5)P_2 (80:10:10). The systems were solvated with water beads and 150 mM NaCl. A total of 16 initial orientations of the protein were generated by rotating the protein around the x or the y axis (with z being the normal of the membrane).

Molecular dynamics (MD) simulations

Coarse-grained MD simulations

Coarse-grained MD simulations were performed with Gromacs 2016 or 2018 using the Martini 2.2 force field (de Jong et al., 2013) or the open beta version of the Martini 3 (3.b3.2) force field (Souza and Marrink, 2020). For the PRLR-TMD-ICD$_{K235-L284}$ simulations we increased the strength of interactions between protein and water by 10% to avoid excessive compaction of the disordered regions, as has been previously done for IDPs and multi-domain proteins (Kassem et al., 2021; Larsen et al., 2020; Thomasen et al., 2022). Other simulation parameters, common to all the CG simulations performed, were chosen following the recommendations in (de Jong et al., 2016). Briefly, a time step of 20 fs was used, the Verlet cut-off scheme was used considering a buffer tolerance of 0.005 kJ/(mol ps atom). The reaction-field method was used for Coulomb interactions with a cut-off of 11 Å and a relative permittivity of ε_r = 15. For van der Waals' interactions, a cut-off of 11 Å was used. The velocity rescaling thermostat was employed with a reference temperature of T = 310 K, with a coupling constant of τ_T = 1 ps. For the equilibrations, the Berendsen barostat was employed (p = 1 bar, τ_p = 3 ps), whereas the production runs were performed with a Parrinello-Rahman barostat (p = 1 bar, τ_p = 12 ps). A semi-isotropic pressure coupling was used for all the systems that contained a lipid bilayer. For all systems, an initial round of equilibration with decreasing constraints applied to the protein beads and lipid beads was performed following the protocol provided by CHARMM-GUI Martini maker module. For the PRLR-TMD-ICD$_{K235-L284}$ simulations, a total of 11 µs of unconstrained MD were performed of which the first microsecond was considered as equilibration and the last 10 µs as production and used for analysis. For the JAK2-FERM-SH2 and the complex between JAK2-FERM-SH2 in solution, 1 µs of unconstrained simulation was performed. In the case of JAK2-FERM-SH2 or the complex between JAK2-FERM-SH2 and PRLR-TMD-ICD$_{K235-L284}$ near a lipid bilayer, an unconstrained run of 5 µs was performed for each system and the complete trajectory considered for analysis.

All-atom molecular dynamics simulations

All-atom MD simulations were performed using GROMACS 2016 and 2018 (Abraham et al., 2015), using the CHARMM36m force field (Huang et al., 2017) for proteins and the TIP3P model for water. The initial system was minimized followed by position restrained simulation in two different phases, NVT and NPT. A 150 ns run of unconstrained NPT equilibration was then performed. The Berendsen thermostat was used for the constrained relaxation runs and the Nose-Hoover thermostat for the production runs. In all cases, the temperature was 310 K. For the NPT simulations, the Berendsen

barostat was used during relaxations and the Parinello-Rahman barostat used in unconstrained production runs. In all cases the target pressure was 1 atm. In all the simulations, the Verlet-cutoff scheme was used with a 2 fs timestep. A cutoff of 12 Å with a switching function starting at 10 Å was used for non-bonded interactions along with periodic boundary conditions. The Particle Mesh Ewald method was used to compute long-range electrostatic forces. Hydrogen atoms were constrained using the LINCS (Hess et al., 1997) algorithm.

Trajectory analyses

Analysis of the obtained trajectories was performed using VMD plugins, GROMACS analysis tools and in-house prepared tcl and python scripts, available on github (see below). For the characterization of the orientation of the JAK2-FERM-SH2+PRLR-ICD$_{K235-E284}$ complex with respect to the lipid bilayer we used the geographical coordinate system with latitude and longitude devised by Herzog et al. (Herzog et al., 2017). Lipid densities were calculated with the Volmap plugin from VMD considering only the PO4 beads and a 1Å grid. Density plots are shown as an enrichment score with values representing the percentage of enrichment or depletion with respect to the average value on the system as done previously in (Corradi et al., 2018). All molecular renderings were done with VMD (Humphrey et al., 1996). Protein-protein contact maps were calculated using CONAN (Mercadante et al., 2018).

Acknowledgements

The authors thank the SYNERGY, BRAINSTRUC and REPIN consortia for valuable discussion and Signe A. Sjørup and Katrine Franklin Mark for skilled technical assistance. We are grateful to Dr. Julie Schnipper for generating the AP1-2PH-PLCδ-GFP cells and to Prof. Vincent Goffin for initial discussions regarding the importance of the KxK-motifs in PRLR.

Additional information

Funding

Funder	*Grant reference number*	*Author*
Novo Nordisk Foundation	NNF18OC0033926	Birthe B. Kragelund
Novo Nordisk Foundation	NNF15OC0016670	Birthe B. Kragelund, Stine F. Pedersen, Lise Arleth
Lundbeck Foundation	BRAINSTRUC	Kresten Lindorff-Larsen, Lise Arleth, Birthe B. Kragelund

The funders had no role in study design, data collection and interpretation, or the decision to submit the work for publication

Author contributions

Raul Araya-Secchi, Formal analysis, Validation, Investigation, Visualization, Methodology, Writing - original draft; **Katrine Bugge**, Formal analysis, Validation, Investigation, Visualization, Methodology, Writing - review and editing; **Pernille Seiffert,** Investigation, Visualization, Methodology, Writing - original draft, Writing - review and editing; **Amalie Petry**, Investigation; **Gitte W. Haxholm,** Investigation, **Kresten Lindorff-Larsen**, Validation, Supervision, Writing -

review and editing, Funding; **Stine F. Pedersen**, Conceptualization, Resources, Formal analysis, Supervision, Funding acquisition, Writing - review and editing;; **Lise Arleth,** Conceptualization, Writing - review and editing; Resources, Formal analysis, Supervision, Funding acquisition; **Birthe B. Kragelund**, Conceptualization, Formal analysis, Validation, Resources, Formal analysis, Visualization, Supervision, Funding acquisition analysis, Writing - original draft, Writing - review and editing;

Author ORCIDs
Raul Araya-Secchi https://orcid.org/0000-0002-4872-3553
Katrine Bugge https://orcid.org/0000-0002-6286-6243
Pernille Seiffert https://orcid.org/0000-0003-4213-5336
Amalie Petry
Gitte W. Haxholm
Kresten Lindorff-Larsen https://orcid.org/0000-0002-4750-6039
Stine Falsig Pedersen https://orcid.org/0000-0002-3044-7714
Lise Arleth https://orcid.org/0000-0002-4694-4299
Birthe B. Kragelund https://orcid.org/0000-0002-7454-1761

Additional files

Supplementary files
MDAR checklist

Data availability
All data needed to evaluate the conclusions in the paper are present in the paper and/or the Supplementary Materials. The MD data and models together with the scripts used in the trajectory analysis are available on Github at https://github.com/Niels-Bohr-Institute-XNS-StructBiophys/PRLRmodel. NMR chemical shifts for the GHR-ICD-LID1 are deposited in the BioMagResBank under the accession number 51695.

REFERENCES

Abraham MJ, Murtola T, Schulz R, Páll S, Smith JC, Hess B, Lindahl E. 2015. GROMACS: High performance molecular simulations through multi-level parallelism from laptops to supercomputers. *SoftwareX* **1–2**:19–25. doi:10.1016/j.softx.2015.06.001

Aksamitiene E, Achanta S, Kolch W, Kholodenko BN, Hoek JB, Kiyatkin A. 2011. Prolactin-stimulated activation of ERK1 / 2 mitogen-activated protein kinases is controlled by PI3-kinase / Rac / PAK signaling pathway in breast cancer cells. *Cell Signal* **23**:1794–1805. doi:10.1016/j.cellsig.2011.06.014

Ashkenazy H, Abadi S, Martz E, Chay O, Mayrose I, Pupko T, Ben-Tal N. 2016. ConSurf 2016: an improved methodology to estimate and visualize evolutionary conservation in macromolecules. *Nucleic Acids Res* **44**:W344-50. doi:10.1093/nar/gkw408

963 Bachelot A, Binart N. 2007. Reproductive role of prolactin. *Reproduction* **133**:361–369.
964 doi:10.1530/REP-06-0299
965 Bocharov E V., Lesovoy DM, Bocharova O V., Urban AS, Pavlov K V., Volynsky PE, Efremov
966 RG, Arseniev AS. 2018. Structural basis of the signal transduction via transmembrane domain
967 of the human growth hormone receptor. *Biochimica et Biophysica Acta (BBA) - General*
968 *Subjects* **1862**:1410–1420. doi:10.1016/j.bbagen.2018.03.022
969 Bole-Feysot C, Goffin V, Edery M, Binart N, Kelly PA. 1998. Prolactin (PRL) and its receptor:
970 actionm signal transduction pathways and phenotypes observed in PRL receptor knockout
971 mice. *Endocr Rev* **19**:225–268.
972 Bompard G, Martin M, Roy C, Vignon F, Freiss G. 2003. Membrane targeting of protein tyrosine
973 phosphatase PTPL1 through its FERM domain via binding to phosphatidylinositol 4,5-
974 biphosphate. *J Cell Sci* **116**:2519–30. doi:10.1242/jcs.00448
975 Boutin JM, Jolicoeur C, Okamura H, Gagnon J, Edery M, Shirota M, Banville D, Dusanter-Fourt I,
976 Djiane J, Kelly PA. 1988. Cloning and expression of the rat prolactin receptor, a member of
977 the growth hormone/prolactin receptor gene family. *Cell* **53**:69–77. doi:10.1016/0092-
978 8674(88)90488-6
979 Brooks AJ, Dai W, O'Mara ML, Abankwa D, Chhabra Y, Pelekanos R a, Gardon O, Tunny K a,
980 Blucher KM, Morton CJ, Parker MW, Sierecki E, Gambin Y, Gomez G a, Alexandrov K,
981 Wilson I a, Doxastakis M, Mark AE, Waters MJ. 2014. Mechanism of Activation of Protein
982 Kinase JAK2 by the Growth Hormone Receptor. *Science (1979)* **344**:1249783–1249783.
983 doi:10.1126/science.1249783
984 Brooks AJ, Dehkhoda F, Kragelund BB. 2016. Cytokine Receptors. *Principles of Endocrinology*
985 *and Hormone Action*. doi:10.1007/978-3-319-27318-1
986 Broutin I, Jomain J-B, Tallet E, van Agthoven J, Raynal B, Hoos S, Kragelund BB, Kelly P a,
987 Ducruix A, England P, Goffin V. 2010. Crystal structure of an affinity-matured prolactin
988 complexed to its dimerized receptor reveals the topology of hormone binding site 2. *J Biol*
989 *Chem* **285**:8422–33. doi:10.1074/jbc.M109.089128
990 Brown RJ, Adams JJ, Pelekanos RA, Wan Y, McKinstry WJ, Palethorpe K, Seeber RM, Monks
991 TA, Eidne KA, Parker MW, Waters MJ. 2005. Model for growth hormone receptor activation
992 based on subunit rotation within a receptor dimer. *Nat Struct Mol Biol* **12**:814–821.
993 doi:10.1038/nsmb977
994 Bugge K, Papaleo E, Haxholm GW, Hopper JTS, Robinson C v, Olsen JG, Lindorff-Larsen K,
995 Kragelund BB. 2016. A combined computational and structural model of the full-length
996 human prolactin receptor. *Nat Commun* **7**:11578. doi:10.1038/ncomms11578
997 Bugge K, Steinocher H, Brooks AJ, Lindor K, Kragelund BB. 2015. Exploiting Hydrophobicity for
998 Efficient Production of Transmembrane Helices for Structure Determination by NMR
999 Spectroscopy. *Anal Chem* **87**:9126–9131. doi:10.1021/acs.analchem.5b02365
1000 Campbell GS, Argetsinger LS, Ihle JN, Kelly PA, Rillema JA, Carter-Su C. 1994. Activation of
1001 JAK2 tyrosine kinase by prolactin receptors in Nb2 cells and mouse mammary gland explants.
1002 *Proceedings of the National Academy of Sciences* **91**:5232–5236. doi:10.1073/pnas.91.12.5232
1003 Carracedo A, Pandolfi PP. 2008. The PTEN–PI3K pathway: of feedbacks and cross-talks.
1004 *Oncogene* **27**:5527–5541. doi:10.1038/onc.2008.247
1005 Chhabra Y, Seiffert P, Gormal RS, Vullings M, Lee CMM, Wallis TP, Dehkhoda F, Indrakumar S,
1006 Jacobsen NL, Lindorff-Larsen K, Durisic N, Waters MJ, Meunier FA, Kragelund BB, Brooks
1007 AJ. n.d. Tyrosine kinases compete for growth hormone receptor binding and regulate receptor
1008 mobility and degradation. *Submitted*.
1009 Clevenger C v, Rui H. 2022. Breast Cancer and Prolactin – New Mechanisms and Models.
1010 *Endocrinology* **163**. doi:10.1210/endocr/bqac122

1011 Corradi V, Mendez-Villuendas E, Ingólfsson HI, Gu R-X, Siuda I, Melo MN, Moussatova A,
1012 DeGagné LJ, Sejdiu BI, Singh G, Wassenaar TA, Delgado Magnero K, Marrink SJ, Tieleman
1013 DP. 2018. Lipid–Protein Interactions Are Unique Fingerprints for Membrane Proteins. *ACS*
1014 *Cent Sci* **4**:709–717. doi:10.1021/acscentsci.8b00143
1015 Dadhich R, Kapoor S. 2022. Lipidomic and Membrane Mechanical Signatures in Triple-Negative
1016 Breast Cancer: Scope for Membrane-Based Theranostics. *Mol Cell Biochem*.
1017 doi:10.1007/s11010-022-04459-4
1018 de Jong DH, Baoukina S, Ingólfsson HI, Marrink SJ. 2016. Martini straight: Boosting performance
1019 using a shorter cutoff and GPUs. *Comput Phys Commun* **199**:1–7.
1020 doi:10.1016/j.cpc.2015.09.014
1021 de Jong DH, Singh G, Bennett WFD, Arnarez C, Wassenaar TA, Schäfer L V., Periole X, Tieleman
1022 DP, Marrink SJ. 2013. Improved Parameters for the Martini Coarse-Grained Protein Force
1023 Field. *J Chem Theory Comput* **9**:687–697. doi:10.1021/ct300646g
1024 de Vos AM, Ultsch M, Kossiakoff AA. 1992. Human growth hormone and extracellular domain of
1025 its receptor: crystal structure of the complex. *Science* **255**:306–12.
1026 Delaglio F, Grzesiek S, Vuister GW, Zhu G, Pfeifer J, Bax A. 1995. NMRPipe: a multidimensional
1027 spectral processing system based on UNIX pipes. *J Biomol NMR* **6**:277–93.
1028 Delaglio Frank, Grzesiek S, Vuister GW, Zhu G, Pfeifer J, Bax A. 1995. NMRPipe: A
1029 multidimensional spectral processing system based on UNIX pipes. *J Biomol NMR* **6**:277–293.
1030 doi:10.1007/BF00197809
1031 Feng J, Mertz B. 2015. Novel phosphotidylinositol 4,5-bisphosphate binding sites on focal adhesion
1032 kinase. *PLoS One* **10**:1–12. doi:10.1371/journal.pone.0132833
1033 Ferrao RD, Wallweber HJA, Lupardus PJ. 2018. Receptor-mediated dimerization of JAK2 FERM
1034 domains is required for JAK2 activation. *Elife* **7**:1–21.
1035 Gadd SL, Clevenger C v. 2006. Ligand-independent dimerization of the human prolactin receptor
1036 isoforms: functional implications. *Mol Endocrinol* **20**:2734–2746. doi:10.1210/me.2006-0114
1037 Glassman CR, Tsutsumi N, Saxton RA, Lupardus PJ, Jude KM, Garcia KC. 2022. Structure of a
1038 Janus kinase cytokine receptor complex reveals the basis for dimeric activation. *Science (1979)*
1039 **376**:163–169. doi:10.1126/science.abn8933
1040 Goñi GM, Epifano C, Boskovic J, Camacho-Artacho M, Zhou J, Bronowska A, Martín MT, Eck
1041 MJ, Kremer L, Gräter F, Gervasio FL, Perez-Moreno M, Lietha D. 2014. Phosphatidylinositol
1042 4,5-bisphosphate triggers activation of focal adhesion kinase by inducing clustering and
1043 conformational changes. *Proc Natl Acad Sci U S A* **111**:E3177-86.
1044 doi:10.1073/pnas.1317022111
1045 Hamada K, Shimizu T, Matsui T, Tsukita S, Hakoshima T. 2000. Structural basis of the membrane-
1046 targeting and unmasking mechanisms of the radixin FERM domain. *EMBO J* **19**:4449–62.
1047 doi:10.1093/emboj/19.17.4449
1048 Hannan FM, Elajnaf T, Vandenberg LN, Kennedy SH, Thakker R v. 2022. Hormonal regulation of
1049 mammary gland development and lactation. *Nat Rev Endocrinol*. doi:10.1038/s41574-022-
1050 00742-y
1051 Haxholm GW, Nikolajsen LF, Olsen JG, Fredsted J, Larsen FH, Goffin V, Pedersen SF, Brooks AJ,
1052 Waters MJ, Kragelund BB. 2015. Intrinsically disordered cytoplasmic domains of two
1053 cytokine receptors mediate conserved interactions with membranes. *Biochem J* **468**:495–506.
1054 doi:10.1042/BJ20141243
1055 Hedger G, Sansom MSP, Koldsø H. 2015a. The juxtamembrane regions of human receptor tyrosine
1056 kinases exhibit conserved interaction sites with anionic lipids. *Sci Rep* **5**:9198.
1057 doi:10.1038/srep09198

Hedger G, Sansom MSP, Koldsø H. 2015b. The juxtamembrane regions of human receptor tyrosine kinases exhibit conserved interaction sites with anionic lipids. *Sci Rep* **5**:9198. doi:10.1038/srep09198

Herzog FA, Braun L, Schoen I, Vogel V. 2017. Structural Insights How PIP2 Imposes Preferred Binding Orientations of FAK at Lipid Membranes. *J Phys Chem B* **121**:3523–3535. doi:10.1021/acs.jpcb.6b09349

Hess B, Bekker H, Berendsen HJC, Fraaije JGEM. 1997. LINCS: A linear constraint solver for molecular simulations. *J Comput Chem* **18**:1463–1472. doi:10.1002/(SICI)1096-987X(199709)18:12<1463::AID-JCC4>3.0.CO;2-H

Huang J, Rauscher S, Nawrocki G, Ran T, Feig M, de Groot BL, Grubmüller H, MacKerell AD. 2017. CHARMM36m: an improved force field for folded and intrinsically disordered proteins. *Nat Methods* **14**:71–73. doi:10.1038/nmeth.4067

Humphrey W, Dalke A, Schulten K. 1996. VMD: Visual molecular dynamics. *J Mol Graph* **14**:33–38. doi:10.1016/0263-7855(96)00018-5

Jo S, Cheng X, Islam SM, Huang L, Rui H, Zhu A, Lee HS, Qi Y, Han W, Vanommeslaeghe K, MacKerell AD, Roux B, Im W. 2014. CHARMM-GUI PDB Manipulator for Advanced Modeling and Simulations of Proteins Containing Nonstandard Residues. pp. 235–265. doi:10.1016/bs.apcsb.2014.06.002

Jo S, Kim T, Iyer VG, Im W. 2008. CHARMM-GUI: A web-based graphical user interface for CHARMM. *J Comput Chem* **29**:1859–1865. doi:10.1002/jcc.20945

Jumper J, Evans R, Pritzel A, Green T, Figurnov M, Ronneberger O, Tunyasuvunakool K, Bates R, Žídek A, Potapenko A, Bridgland A, Meyer C, Kohl SAA, Ballard AJ, Cowie A, Romera-Paredes B, Nikolov S, Jain R, Adler J, Back T, Petersen S, Reiman D, Clancy E, Zielinski M, Steinegger M, Pacholska M, Berghammer T, Bodenstein S, Silver D, Vinyals O, Senior AW, Kavukcuoglu K, Kohli P, Hassabis D. 2021. Highly accurate protein structure prediction with AlphaFold. *Nature* **596**:583–589. doi:10.1038/s41586-021-03819-2

Kassem N, Araya-Secchi R, Bugge K, Barclay A, Steinocher H, Khondker A, Wang Y, Lenard AJ, Bürck J, Sahin C, Ulrich AS, Landreh M, Pedersen MC, Rheinstädter MC, Pedersen PA, Lindorff-Larsen K, Arleth L, Kragelund BB. 2021. Order and disorder—An integrative structure of the full-length human growth hormone receptor. *Sci Adv* **7**:eabh3805. doi:10.1126/sciadv.abh3805

Kjaergaard M, Brander S, Poulsen FM. 2011. Random coil chemical shift for intrinsically disordered proteins: Effects of temperature and pH. *J Biomol NMR* **49**:139–149. doi:10.1007/s10858-011-9472-x

Kjaergaard M, Kragelund BB. 2017. Functions of intrinsic disorder in transmembrane proteins. *Cellular and Molecular Life Sciences* **74**:3205–3224. doi:10.1007/s00018-017-2562-5

Kubatzky KF, Ruan W, Gurezka R, Cohen J, Ketteler R, Watowich SS, Neumann D, Langosch D, Klingmüller U. 2001. Self assembly of the transmembrane domain promotes signal transduction through the erythropoietin receptor. *Current Biology* **11**:110–115. doi:10.1016/S0960-9822(01)00018-5

Landau M, Mayrose I, Rosenberg Y, Glaser F, Martz E, Pupko T, Ben-Tal N. 2005. ConSurf 2005: the projection of evolutionary conservation scores of residues on protein structures. *Nucleic Acids Res* **33**:W299-302. doi:10.1093/nar/gki370

Larsen AH, Wang Y, Bottaro S, Grudinin S, Arleth L, Lindorff-Larsen K. 2020. Combining molecular dynamics simulations with small-angle X-ray and neutron scattering data to study multi-domain proteins in solution. *PLoS Comput Biol* **16**:e1007870. doi:10.1371/journal.pcbi.1007870

1105 Lee J, Cheng X, Swails JM, Yeom MS, Eastman PK, Lemkul JA, Wei S, Buckner J, Jeong JC, Qi
1106 Y, Jo S, Pande VS, Case DA, Brooks CL, MacKerell AD, Klauda JB, Im W. 2016.
1107 CHARMM-GUI Input Generator for NAMD, GROMACS, AMBER, OpenMM, and
1108 CHARMM/OpenMM Simulations Using the CHARMM36 Additive Force Field. *J Chem*
1109 *Theory Comput* **12**:405–413. doi:10.1021/acs.jctc.5b00935
1110 Lu J, Dong W, Hammond GR, Hong Y. 2022. Hypoxia controls plasma membrane targeting of
1111 polarity proteins by dynamic turnover of PI4P and PI(4,5)P2. *Elife* **11**.
1112 doi:10.7554/eLife.79582
1113 Maeda R, Sato T, Okamoto K, Yanagawa M, Sako Y. 2018. Lipid-Protein Interplay in Dimerization
1114 of Juxtamembrane Domains of Epidermal Growth Factor Receptor. *Biophys J* **114**:893–903.
1115 doi:10.1016/j.bpj.2017.12.029
1116 Mani T, Hennigan RF, Foster LA, Conrady DG, Herr AB, Ip W. 2011. FERM Domain
1117 Phosphoinositide Binding Targets Merlin to the Membrane and Is Essential for Its Growth-
1118 Suppressive Function. *Mol Cell Biol* **31**:1983–1996. doi:10.1128/MCB.00609-10
1119 Mayzel M, Rosenlo J, Orekhov VY. 2014. Time-resolved multidimensional NMR with non-
1120 uniform sampling. *J Biomol NMR* **58**:129–139. doi:10.1007/s10858-013-9811-1
1121 McLaughlin S, Smith SO, Hayman MJ, Murray D. 2005. An Electrostatic Engine Model for
1122 Autoinhibition and Activation of the Epidermal Growth Factor Receptor (EGFR/ErbB)
1123 Family. *Journal of General Physiology* **126**:41–53. doi:10.1085/jgp.200509274
1124 McLaughlin S, Wang J, Gambhir A, Murray D. 2002. PIP(2) and proteins: interactions,
1125 organization, and information flow. *Annu Rev Biophys Biomol Struct* **31**:151–75.
1126 doi:10.1146/annurev.biophys.31.082901.134259
1127 McNally R, Toms A V., Eck MJ. 2016. Crystal Structure of the FERM-SH2 Module of Human
1128 Jak2. *PLoS One* **11**:e0156218. doi:10.1371/journal.pone.0156218
1129 Mercadante D, Gräter F, Daday C. 2018. CONAN: A Tool to Decode Dynamical Information from
1130 Molecular Interaction Maps. *Biophys J* **114**:1267–1273. doi:10.1016/j.bpj.2018.01.033
1131 Metcalf DG, Moore DT, Wu Y, Kielec JM, Molnar K, Valentine KG, Wand AJ, Bennett JS,
1132 DeGrado WF. 2010. NMR analysis of the αIIbβ3 cytoplasmic interaction suggests a
1133 mechanism for integrin regulation. *Proceedings of the National Academy of Sciences*
1134 **107**:22481–22486. doi:10.1073/pnas.1015545107
1135 Morris R, Kershaw NJ, Babon JJ. 2018. The molecular details of cytokine signaling via the
1136 JAK/STAT pathway. *Protein Science* **27**:1984–2009. doi:10.1002/pro.3519
1137 Newey PJ, Gorvin CM, Cleland SJ, Willberg CB, Bridge M, Azharuddin M, Drummond RS, van
1138 der Merwe PA, Klenerman P, Bountra C, Thakker R v. 2013. Mutant Prolactin Receptor and
1139 Familial Hyperprolactinemia. *New England Journal of Medicine* **369**:2012–2020.
1140 doi:10.1056/NEJMoa1307557
1141 Orekhov VY, Jaravine VA. 2011. Analysis of non-uniformly sampled spectra with multi-
1142 dimensional decomposition. *Prog Nucl Magn Reson Spectrosc* **59**:271–292.
1143 doi:10.1016/j.pnmrs.2011.02.002
1144 Park MJ, Sheng R, Silkov A, Jung DJ, Wang ZG, Xin Y, Kim H, Thiagarajan-Rosenkranz P, Song
1145 S, Yoon Y, Nam W, Kim I, Kim E, Lee DG, Chen Y, Singaram I, Wang L, Jang MH, Hwang
1146 CS, Honig B, Ryu S, Lorieau J, Kim YM, Cho W. 2016. SH2 Domains Serve as Lipid-Binding
1147 Modules for pTyr-Signaling Proteins. *Mol Cell* **62**. doi:10.1016/j.molcel.2016.01.027
1148 Patwardhan P, Resh MD. 2010. Myristoylation and membrane binding regulate c-Src stability and
1149 kinase activity. *Mol Cell Biol* **30**:4094–4107. doi:10.1128/MCB.00246-10
1150 Pettersen EF, Goddard TD, Huang CC, Couch GS, Greenblatt DM, Meng EC, Ferrin TE. 2004.
1151 UCSF Chimera - A visualization system for exploratory research and analysis. *J Comput Chem*
1152 **25**:1605–1612. doi:10.1002/jcc.20084

1153 Pezet A, Buteau H, Kelly PA, Edery M. 1997. The last proline of Box 1 is essential for association
1154 with JAK2 and functional activation of the prolactin receptor. *Mol Cell Endocrinol* **129**:199–
1155 208. doi:10.1016/S0303-7207(97)00063-4
1156 Qi Y, Ingólfsson HI, Cheng X, Lee J, Marrink SJ, Im W. 2015. CHARMM-GUI Martini Maker for
1157 Coarse-Grained Simulations with the Martini Force Field. *J Chem Theory Comput* **11**:4486–
1158 4494. doi:10.1021/acs.jctc.5b00513
1159 Rawat A, Harishchandran A, Nagaraj R. 2013. Fatty acyl chain-dependent but charge-independent
1160 association of the SH4 domain of Lck with lipid membranes. *J Biosci* **38**:63–71.
1161 doi:10.1007/s12038-012-9288-1
1162 Rawat A, Nagaraj R. 2010. Determinants of membrane association in the SH4 domain of Fyn: roles
1163 of N-terminus myristoylation and side-chain thioacylation. *Biochim Biophys Acta* **1798**:1854–
1164 63. doi:10.1016/j.bbamem.2010.06.009
1165 Roberts E, Eargle J, Wright D, Luthey-Schulten Z. 2006. MultiSeq: unifying sequence and structure
1166 data for evolutionary analysis. *BMC Bioinformatics* **7**:382. doi:10.1186/1471-2105-7-382
1167 Rowlinson SW, Yoshizato H, Barclay JL, Brooks AJ, Behncken SN, Kerr LM, Millard K,
1168 Palethorpe K, Nielsen K, Clyde-Smith J, Hancock JF, Waters MJ. 2008. An agonist-induced
1169 conformational change in the growth hormone receptor determines the choice of signalling
1170 pathway. *Nat Cell Biol* **10**:740–7. doi:10.1038/ncb1737
1171 Rui H, Kirken RA, Farrar WL. 1994. Activation of receptor-associated tyrosine kinase JAK2 by
1172 prolactin. *J Biol Chem* **269**:5364–8.
1173 Russell RB, Barton GJ. 1992. Multiple protein sequence alignment from tertiary structure
1174 comparison: Assignment of global and residue confidence levels. *Proteins: Structure,*
1175 *Function, and Genetics* **14**:309–323. doi:10.1002/prot.340140216
1176 Sackmann-Sala L, Goffin V. 2015. Prolactin-Induced Prostate Tumorigenesis. pp. 221–242.
1177 doi:10.1007/978-3-319-12114-7_10
1178 Seiffert P, Bugge K, Nygaard M, Haxholm GW, Martinsen JH, Pedersen MN, Arleth L, Boomsma
1179 W, Kragelund BB. 2020. Orchestration of signaling by structural disorder in class 1 cytokine
1180 receptors. *Cell Communication and Signaling* **18**. doi:10.1186/s12964-020-00626-6
1181 Seubert N, Royer Y, Staerk J, Kubatzky KF, Moucadel V, Krishnakumar S, Smith SO,
1182 Constantinescu SN. 2003. Active and Inactive Orientations of the Transmembrane and
1183 Cytosolic Domains of the Erythropoietin Receptor Dimer. *Mol Cell* **12**:1239–1250.
1184 Shen M-Y, Sali A. 2006. Statistical potential for assessment and prediction of protein structures.
1185 *Protein Sci* **15**:2507–24. doi:10.1110/ps.062416606
1186 Sheng R, Jung DJ, Silkov A, Kim H, Singaram I, Wang ZG, Xin Y, Kim E, Park MJ, Thiagarajan-
1187 Rosenkranz P, Smrt S, Honig B, Baek K, Ryu S, Lorieau J, Kim YM, Cho W. 2016. Lipids
1188 regulate Lck protein activity through their interactions with the Lck Src homology 2 domain.
1189 *Journal of Biological Chemistry* **291**:17639–17650. doi:10.1074/jbc.M116.720284
1190 Souza PCT, Marrink SJS. 2020. Martini 3 - Open Beta-Release. *http://cgmartini.nl*.
1191 Suh BC, Hille B. 2005. Regulation of ion channels by phosphatidylinositol 4,5-bisphosphate. *Curr*
1192 *Opin Neurobiol* **15**:370–378. doi:10.1016/J.CONB.2005.05.005
1193 Thomasen FE, Pesce F, Roesgaard MA, Tesei G, Lindorff-Larsen K. 2022. Improving Martini 3 for
1194 Disordered and Multidomain Proteins. *J Chem Theory Comput* **18**:2033–2041.
1195 doi:10.1021/acs.jctc.1c01042
1196 Trimble WS, Grinstein S. 2015. Barriers to the free diffusion of proteins and lipids in the plasma
1197 membrane. *Journal of Cell Biology* **208**:259–271. doi:10.1083/jcb.201410071
1198 van den Bogaart G, Meyenberg K, Risselada HJ, Amin H, Willig KI, Hubrich BE, Dier M, Hell
1199 SW, Grubmüller H, Diederichsen U, Jahn R. 2011. Membrane protein sequestering by ionic
1200 protein–lipid interactions. *Nature* **479**:552–555. doi:10.1038/nature10545

1201 Varadi M, Anyango S, Deshpande M, Nair S, Natassia C, Yordanova G, Yuan D, Stroe O, Wood G,
1202 Laydon A, Žídek A, Green T, Tunyasuvunakool K, Petersen S, Jumper J, Clancy E, Green R,
1203 Vora A, Lutfi M, Figurnov M, Cowie A, Hobbs N, Kohli P, Kleywegt G, Birney E, Hassabis
1204 D, Velankar S. 2022. AlphaFold Protein Structure Database: massively expanding the
1205 structural coverage of protein-sequence space with high-accuracy models. *Nucleic Acids Res*
1206 **50**:D439–D444. doi:10.1093/nar/gkab1061
1207 Vranken WF, Boucher W, Stevens TJ, Fogh RH, Pajon A, Llinas M, Ulrich EL, Markley JL,
1208 Ionides J, Laue ED. 2005. The CCPN data model for NMR spectroscopy: Development of a
1209 software pipeline. *Proteins: Structure, Function, and Bioinformatics* **59**:687–696.
1210 doi:10.1002/prot.20449
1211 Wallweber HJA, Tam C, Franke Y, Starovasnik MA, Lupardus PJ. 2014. Structural basis of
1212 recognition of interferon-α receptor by tyrosine kinase 2. *Nat Struct Mol Biol* **21**:443–448.
1213 doi:10.1038/nsmb.2807
1214 Webb B, Sali A. 2016. Comparative Protein Structure Modeling Using MODELLER. *Curr Protoc*
1215 *Bioinformatics* **54**. doi:10.1002/cpbi.3
1216 Wilmes S, Hafer M, Vuorio J, Tucker JA, Winkelmann H, Löchte S, Stanly TA, Pulgar Prieto KD,
1217 Poojari C, Sharma V, Richter CP, Kurre R, Hubbard SR, Garcia KC, Moraga I, Vattulainen I,
1218 Hitchcock IS, Piehler J. 2020. Mechanism of homodimeric cytokine receptor activation and
1219 dysregulation by oncogenic mutations. *Science (1979)* **367**:643–652.
1220 doi:10.1126/science.aaw3242
1221 Yamauchi T, Kaburagi Y, Ueki K, Tsuji Y, Stark GR, Kerr IM, Tsushima T, Akanuma Y, Komuro
1222 I, Tobe K, Yazaki Y, Kadowaki T. 1998. Growth Hormone and Prolactin Stimulate Tyrosine
1223 Phosphorylation of Insulin Receptor Substrate-1, -2, and -3, Their Association with p85
1224 Phosphatidylinositol 3-Kinase (PI3-kinase), and Concomitantly PI3-kinase Activation via
1225 JAK2 Kinase. *Journal of Biological Chemistry* **273**:15719–15726.
1226 doi:10.1074/jbc.273.25.15719
1227 Zhang D, Wlodawer A, Lubkowski J. 2016. Crystal Structure of a Complex of the Intracellular
1228 Domain of Interferon λ Receptor 1 (IFNLR1) and the FERM/SH2 Domains of Human JAK1. *J*
1229 *Mol Biol* **428**:4651–4668. doi:10.1016/j.jmb.2016.10.005
1230
1231
1232 **FIGURE LEGENDS**
1233 **Fig. 1: Schematics of the PRLR:PRL:JAK2 complex in the membrane.** The PRLR is shown in
1234 light blue, the PRL as a dark blue triangle, the PRLR-ICD as a disordered chain and JAK2 in purple.
1235 The lipid PI(4,5)P_2 is shown in orange. The intracellular juxtamembrane (ICJM) region and BOX1
1236 of PRLR-ICD are highlighted in green nuances, while the three LIDs as defined in Haxholm et al.,
1237 (Haxholm et al., 2015) are highlighted in red. For simplicity only one of the two ICDs is shown
1238 associated with JAK2.
1239
1240 **Fig. 2: The ICJM region of the PRLR interacts with PI(4,5)P_2. A)** Overview of investigated PRLR
1241 variants. **B)** Secondary chemical shifts (SCSs) of TMD-$ICD_{F206-S270}$ reconstituted in DHPC micelles.
1242 **C)** Correlation plot of the SCSs of $ICD_{G236-Q396}$ plotted against those of TMD-$ICD_{F206-S270}$. **D) Top**:
1243 Far-UV CD spectra of Pep1 titrated with C_8-PI(4,5)P_2 or in 65% TFE. **Middle:** Far-UV CD spectra
1244 of Pep1 in the presence of 5x-38x C_8-PI(4,5)P_2 subtracted with the spectrum of Pep1 in the absence
1245 of C_8-PI(4,5)P_2. **Bottom**: Far-UV CD spectra of Pep2 titrated with C_8-PI(4,5)P_2 or in 65% TFE**. E)**
1246 ^{15}N,^{1}H-HSQC spectra of ^{15}N-$ICD_{K235-G313}$ titrated with 5x, 10x and 25x molar excess of C_8-PI(4,5)P_2.

1247 **F) Structure of** C_8-PI(4,5)P_2 **G)** Backbone amide chemical shift perturbations (CSPs) and peak
1248 intensity changes upon addition of C_8-PI(4,5)P_2 to ^{15}N-ICD$_{K235-G313}$ plotted against residue number.
1249 **Figure supplement 1**: *^{15}N, ^{1}H-HSQC spectra of A) TMD$_{F206-V240}$ and TMD-ICD$_{F206-S270}$ in DHPC*
1250 *micelles, and (B) TMD-ICD$_{F206-S270}$ in POPC SUVs.*
1251 **Figure supplement 2**: *C^{α} secondary chemical shifts of ICD$_{G236-Q396}$*
1252
1253 **Fig. 3. Protein – lipid interactions of PRLR-ICD$_{LID1}$ obtained from CG-MD simulations**. **(A-F)**
1254 Protein – lipids contact histograms for PRLR-ICD$_{LID1}$ and **A,D**) POPC:POPS(70:30), **B,E)**
1255 POPC:POPS:PI(4,5)P_2 (90:5:5) and **C,F)** POPC:POPS:PI(4,5)P_2 (80:10:10). A contact is counted if
1256 the distance between the backbone beads of the protein is ≤ 7 Å from the head-group beads of the
1257 lipids (A-C) or if the distance between the backbone bead of the protein is ≤ 7 Å from the acyl-chain
1258 bead of the lipids (D-F). **G)** Correlation between the change in NMR signal and the PRLR-ICD$_{LID1}$ –
1259 PI(4,5)P_2 contact frequency from the PRLR-ICD$_{LID1}$ + POPC:POPS:PI(4,5)P_2 (80:10:10) system.
1260 Pearson correlation coefficient of -0.83 with $p = 7.3\text{x}10^{-5}$ and R^2= 0.7. **H)** Average PI(4,5)P_2 density
1261 map (*xy*-plane) taken from the PRLR-ICD$_{LID1}$ + POPC:POPS:PI(4,5)P_2 (80:10:10) simulation. The
1262 map is colored according to the enrichment/depletion percentage with respect to the average density
1263 value. **I)** Schematic representation of how the interactions and the embedment into the membrane of
1264 PRLR contribute to the co-structure formation. The data from the simulations corresponds to those
1265 of the production stage (see methods).
1266 **Figure supplement 1**: *Protein – lipid interactions of PRLR-ICD$_{LID1}$ obtained from CG-MD*
1267 *simulations using the martini 2.2 forcefield.*
1268
1269 **Fig. 4. Protein – lipid interactions of the JAK2-FERM-SH2 PRLR-ICD$_{LID1}$ complex obtained**
1270 **from CG-MD simulations**. **A)** Schematic representation of the simulated system. Combined **B)**
1271 JAK2-FERM-SH2-lipid and **C)** PRLR-ICD$_{LID1}$-lipid contact frequency histograms for the 16 CG
1272 simulations of the JAK2-FERM-SH2 +PRLR-ICD$_{LID1}$+ POPC:POPS:PI(4,5)P_2 system. **D)**
1273 Distribution of the orientations adopted by the JAK2-FERM-SH2 + PRLR-ICD$_{LID1}$ complex when
1274 bound to lipids taken from the 16 simulations with POPC:POPS:PI(4,5)P_2 in the lower-leaflet. The
1275 snapshots surrounding the map correspond to representative conformations of the highlighted states
1276 also indicating the fraction total bound time for which each state was observed. Representative
1277 conformations of **E)** State 2 and **F)** State 4. The grey cylinder depicts the position where PRLR-TMD
1278 should be located. Representative protein-lipid contact histograms for **G)** State2 and **H)** State4
1279 colored as in panels B and C.
1280 **Figure supplement 1**: *Analysis of the JAK2-FERM-SH2- PRLR-ICD$_{LID1}$ AA-MD simulation***.**
1281 **Figure supplement 2.** *Complementary analysis of Protein – lipid interactions of the JAK2-FERM-*
1282 *SH2 PRLR-ICD$_{LID1}$ complex obtained from CG-MD simulations*
1283 **Figure supplement 3.** *Snapshots of the different binding states observed for the JAK2-FERM-SH2 –*
1284 *PRLR-ICD$_{LID1}$ complex with the complete structural model of JAK2*
1285
1286 **Fig. 5. PRLR variants with mutations in lipid interacting residues exhibit decreased PRL-**
1287 **stimulated STAT5 activation in AP1-2PH-PLCδ-GFP cells. A)** NMR intensity changes of
1288 ICD$_{K235-G313}$ WT, K4G, K4E, φ4G and GAG variants upon titration with 5x, 10x and 25x molar

excess C_8-PI(4,5)P_2 plotted against residue number. **B)** The PRLR variants (WT, K4G, K4E, φ4G, 3GAG) were transiently transfected in AP1 cells stably expressing the 2PH-PLCδ-GFP construct which visualizes the plasma membrane by binding PI(4,5)P_2. The cells were subsequently analysed by immunofluorescence microscopy, using antibodies against PRLR (magenta) and GFP (green), as well as DAPI (blue) to mark nuclei. To the right, examples of an average line-scan for each PRLR variant is shown. The fluorescence intensity depicted along the white line drawn (arrow) and green fluorescence (plasma membrane) was used to divide the line in a plasma membrane section and intracellular section, and relative membrane localization was calculated as the average fluorescence of PRLR in the membrane section divided by that in the intracellular section. **C, D)** AP1-2PH-PLCδ-GFP cells were transiently transfected with PRLR variants (WT, K4G, K4E, φ4G, 3GAG, $K2E_{253}$, $K2E_{261}$) and incubated overnight followed by serum starvation for 16-17 h and were subsequently incubated with or without 10 nM prolactin for 30 min. The resulting lysates were analysed by western blot for STAT5, pSTAT5 (Y964), PRLR, β-actin and p150 levels. The immunoblots are representative of three biological replicates. **E**) Ratio of plasma membrane localized receptor compared to intracellular receptor, analysed by line-scans as in B. Each point represents an individual cell, and data are based on three independent biological experiments per condition. Graphs show means with SEM error bars. *P<0.05, **P<0.01 and ****P<0.0001. One-way ANOVA compared to WT, unpaired**. F)** Quantification of western blot results shown as pSTAT5 normalized to total STAT5, relative to the WT condition. Graphs show means with SEM error bars. *P<0.05 and **P<0.01. One-way ANOVA compared to WT, unpaired.

Source file 1: Raw western blots (relating to *figure 5C*)

Source file 2: Raw western blot (relating to *figure 5D*)

Source file 3: Data summaries (relating to *figure 5E,F*)

Figure supplement 1: *Chemical shift perturbations of $ICD_{K235-G313}$ of A) WT, B) K4E, C) GAG, D) K4G and E) ϕ4G variants.*

Figure supplement 2: *^{15}N R_2 relaxation rates of $ICD_{K235-G313}$ of WT (grey bars), K4G (blue dots) and ϕ4G (red squares) variants.*

Fig. 6. Model of how co-structure formation between JAK2, PRLR and PI4(4,5)P_2 may contribute to signalling fidelity. The suggested states in signalling would be **A**) the inactive state of the co-structure exemplified by the Flat orientation. **B**) The hormone bound state expemplfied by the co-structure in the Y orientation. **C**) Phosphorylation of PIP(4,5)P_2 to PI(3,4,5)P_3 for which the PRLR has no affinity may lead to downregulation and/or termination of signalling. The colour scheme of the proteins is identical to Fig.4.

1324 **Figure supplements and Supplementary files**

1325

1326 The prolactin receptor scaffolds Janus kinase 2 via co-structure 1327 formation with phosphoinositide-4,5-bisphosphate

1328 Raul Araya-Secchi[1,2], Katrine Bugge[3#], Pernille Seiffert[3#], Amalie Petry[4], Gitte W. Haxholm[3],
1329 Kresten Lindorff-Larsen[3], Stine F. Pedersen[4*], Lise Arleth[1*] and Birthe B. Kragelund[3*]
1330
1331 [1]Structural Biophysics, Section for Neutron and X-ray Science, Niels Bohr Institute, University of
1332 Copenhagen, 2100 Copenhagen, Denmark.
1333 [2] Facultad de Ingenieria Arquitectura y Diseño, Universidad San Sebastian, Bellavista 7, Santiago,
1334 Chile.
1335 [3]Structural Biology and NMR Laboratory (SBiNLab), Department of Biology, University of
1336 Copenhagen, 2200 Copenhagen, Denmark.
1337 [4]Section for Cell Biology and Physiology, Department of Biology, University of Copenhagen, 2200
1338 Copenhagen N, Denmark
1339
1340

1341 **Overview of contents:**

1342 **Figure supplements for main figures:**

1343 **Figure 2 – Figure supplement** 1: ^{15}N, ^{1}H-HSQCs of $TMD_{F206-V240}$, TMD-$ICD_{F206-S270}$ in DHPC micelles (A)
1344 and TMD-$ICD_{F206-S270}$ in POPC SUVs (B)

1345 **Figure 2 – Figure supplement** 2: Cα secondary chemical shifts of $ICD_{G236-Q396}$

1346 **Figure 3 – Figure supplement** 1: Protein – lipid interactions of PRLR-ICDLID1 obtained from CG-MD
1347 simulations using the martini 2.2 forcefield

1348 **Figure 4 – Figure supplement** 1: Analysis of the JAK2-FERM-SH2- PRLR-ICD_{LID1} AA-MD simulation.

1349 **Figure 4 – Figure supplement** 2: Complementary analysis of Protein – lipid interactions of the JAK2-FERM-
1350 SH2 PRLR-ICDLID1 complex obtained from CG-MD simulations

1351 **Figure 4 – Figure supplement** 3: Snapshots of the different binding states observed for the JAK2-FERM-
1352 SH2 – PRLR-ICDLID1 complex with the complete structural model of JAK2

1353 **Figure 5 – Figure supplement** 1: Chemical shift pertubations of $ICD_{K235-G313}$ of A) WT B) K4E, C) GAG, D)
1354 K4G and E) ϕ4G variants.

1355 **Figure 5 – Figure supplement** 2: ^{15}N R_2 relaxation rates of $ICD_{K235-G313}$ of WT (grey bars), K4G (blue dots)
1356 and ϕ4G (red squares) variants.

Supplementary files not directly related to any main figures:

Movie 1: Y State (STATE 2) from the JAK2-FERM-SH2 PRLR-ICD$_{K235-E284}$ complex simulated near a bilayer containing PI(4,5)P_2 : Representative trajectory showing State 2 (Y). Protein and lipids colored as in Fig. 4

Movie 2: FLAT State (STATE 4) from the JAK2-FERM-SH2 PRLR-ICD$_{K235-E284}$ complex simulated near a bilayer containing PI(4,5)P_2 : Representative trajectory showing State 4 (Y). Protein and lipids colored as in Fig. 4

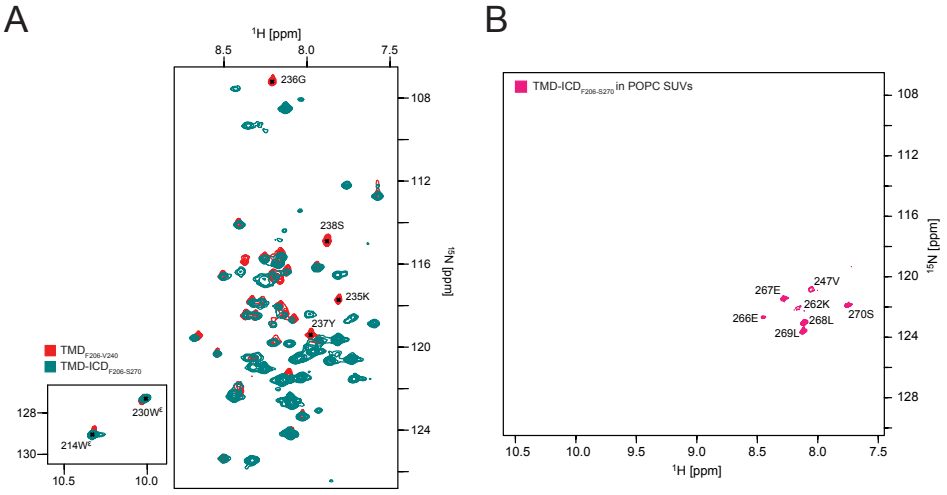

Figure 2 – figure supplement 1. ^{15}N, ^{1}H-HSQC spectra of A) TMD$_{F206-V240}$ and TMD-ICD$_{F206-S270}$ in DHPC micelles, and (B) TMD-ICD$_{F206-S270}$ in POPC SUVs.

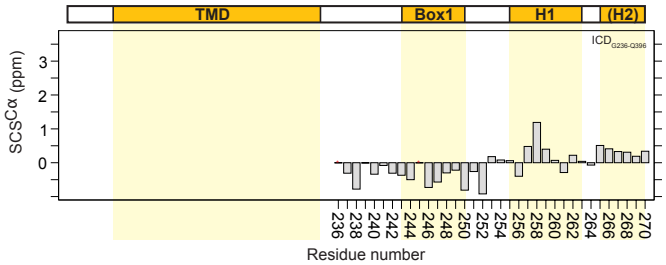

Figure 2 – figure supplement 2. C$^\alpha$ secondary chemical shifts of ICD$_{G236-Q396}$.

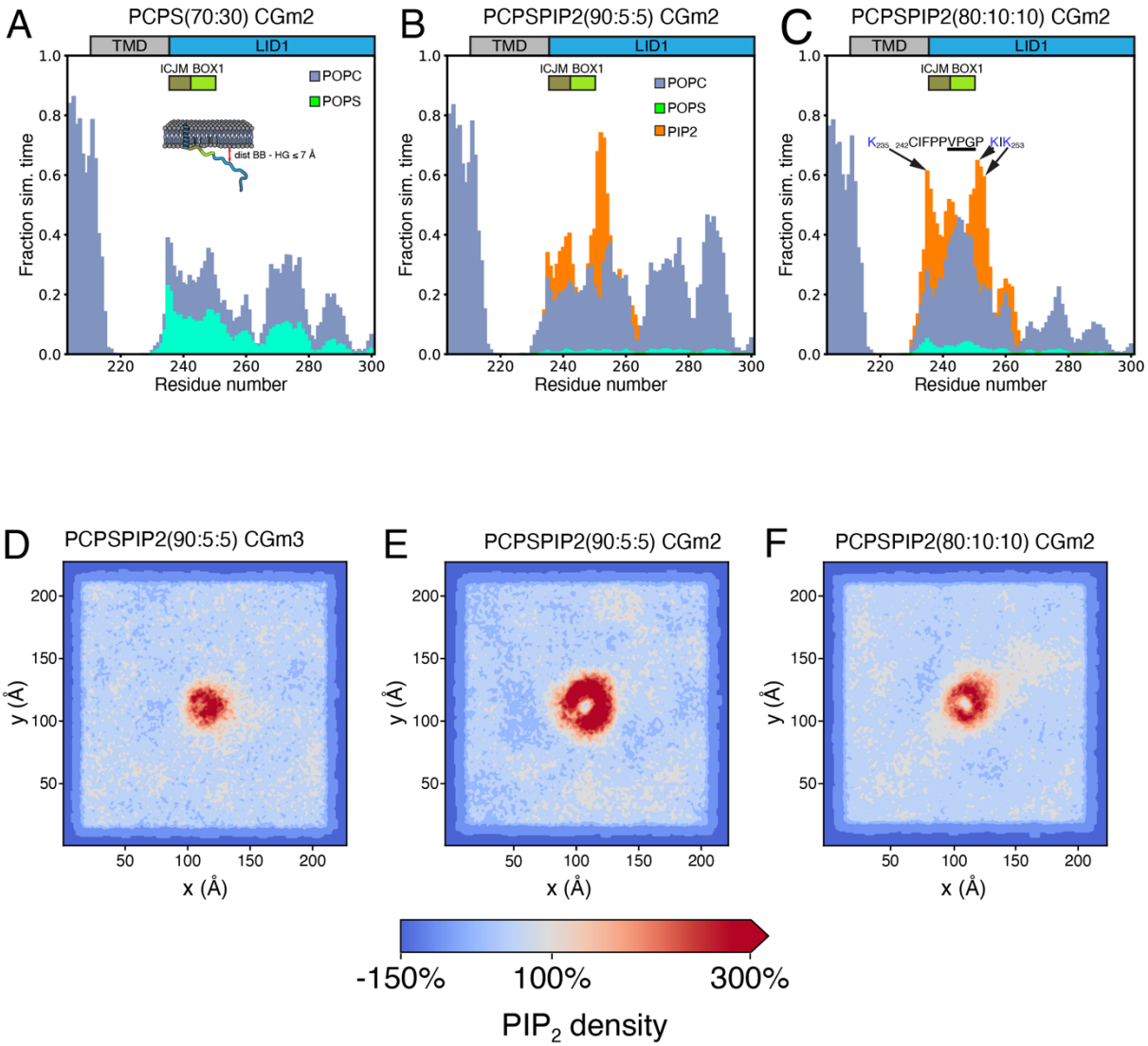

Figure 3 – figure supplement 1. Protein – lipid interactions of PRLR-TMD-ICD$_{G204-H300}$ obtained from CG-MD simulations using the martini 2.2 forcefield. (A-C) Protein – lipids contact histograms between PRLR-ICD$_{K235-E284}$ and A) POPC:POPS(70:30), (B) POPC:POPS:PI(4,5)P_2 (90:5:5) and (C) POPC:POPS:PI(4,5)P_2 (80:10:10) for the simulations performed with the martini 2.2 forcefield (CGm2). The contacts are monitored between the BB of the protein is ≤ 7 Å from the head-group beads of the lipids. (D-F) Average PI(4,5)P_2 density maps (xy-plane) taken from (D) the PRLR-TMD-ICD$_{G204-H300}$ + POPC:POPS:PI(4,5)P_2 (90:5:5) CGm3pws10 simulation; (E) the PRLR-TMD-ICD$_{G204-H300}$ + POPC:POPS:PI(4,5)P_2 (90:5:5) CGm2 simulation

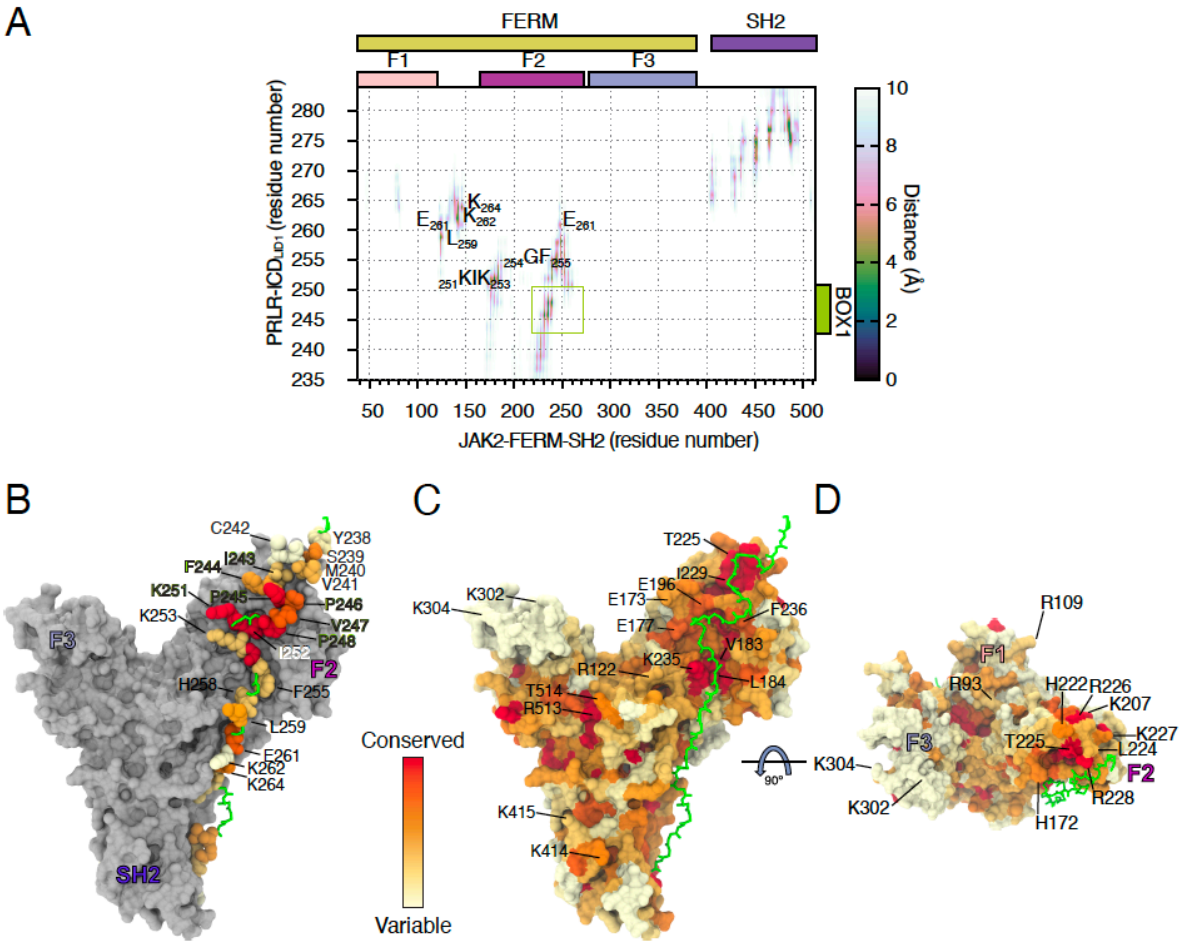

Figure 4 - Figure supplement 1: **Analysis of the JAK2-FERM-SH2- PRLR-ICD$_{K235-H300}$ AA-MD simulation.** A) Average distance map between JAK2-FERM-SH2 and PRLR-ICD$_{K235-H300}$ obtained from the all-atom MD simulation. (B) Conservation of residues from PRLR in contact with JAK2-FERM-SH2 (see A). Residues with green label correspond to BOX1. (C-D) Conservation JAK2-FERM-SH2 oriented as state 2 (see Fig. 4E). Labeled residues correspond to residues that contact PRLR (see A) or that contact the lipids on states 2 and 4 (see Fig. 4E-H).

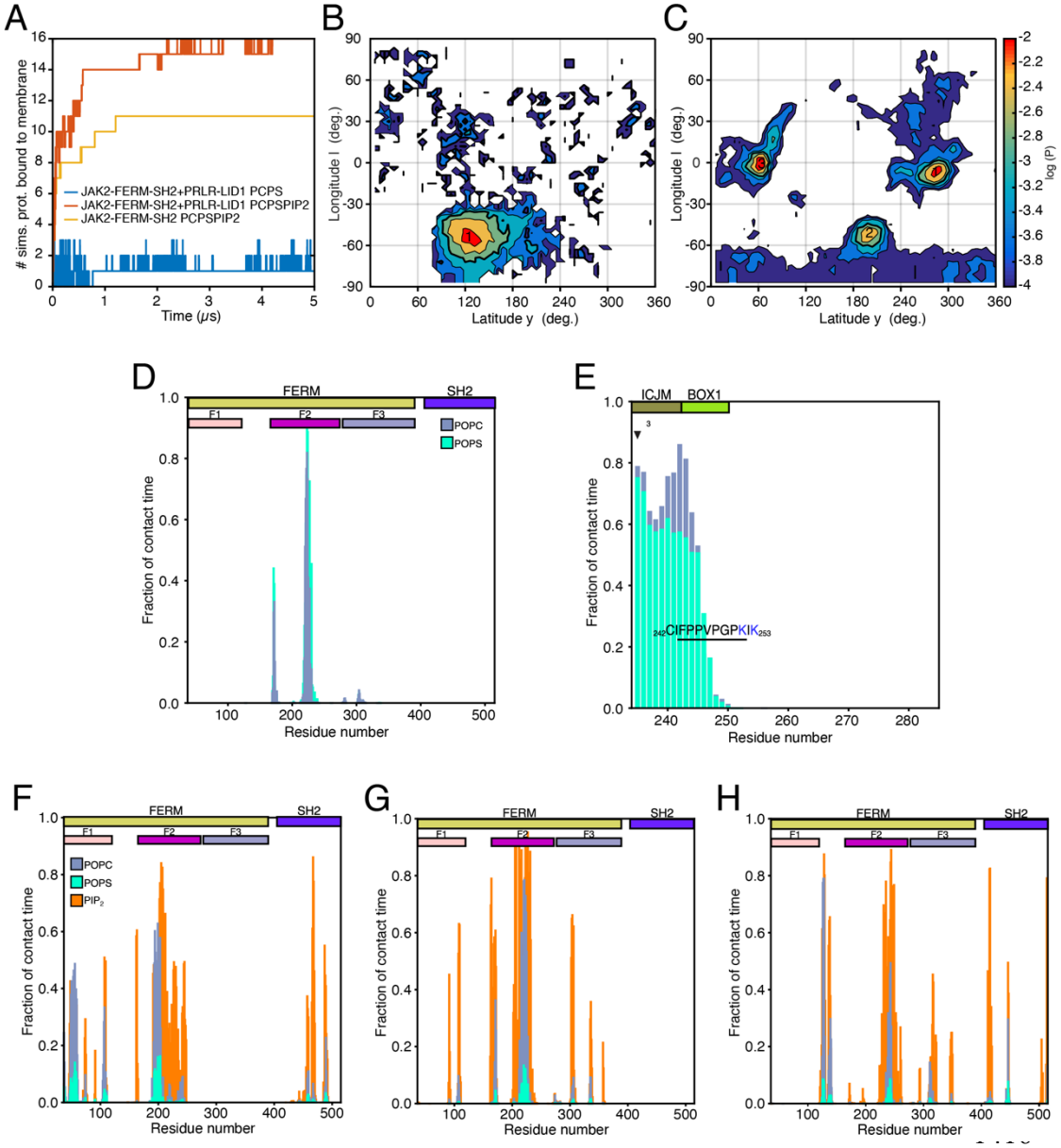

Figure 4 - Figure Supplement 2. Complementary analysis of Protein – lipid interactions of the JAK2-FERM-SH2 PRLR-ICD$_{K235-H300}$ complex obtained from CG-MD simulations (A) Number of simulations where protein is bound to the lower-leaf of the bilayer for the simulations containing: the JAK2-FERM-SH2 + PRLR-ICD$_{K235-H300}$ complex near a POPC:POPS(70:30) bilayer (blue line) and the JAK2-FERM-SH2 + PRLR-ICD$_{K235-H300}$ complex (red line) and the apo JAK2-FERM-SH2 (orange line)near a POPC:POPS:PI(4,5)P_2 (80:10:10) bilayer. (B-C) Distribution of the orientations adopted by (B) the JAK2-FERM-SH2 + PRLR-ICD$_{K235-H300}$ complex when bound to lipids taken from the simulations with POPC:POPS(70:30) in the lower-leaflet and (C) the apo JAK2-FERM-SH2 when bound to lipids taken from the simulations with POPC:POPS:PI(4,5)P_2 (80:10:10) in the lower-leaflet. (D-E) Representative protein-lipid contact histograms for State 1 observed for the JAK2-FERM-SH2 + PRLR- ICD$_{K235-H300}$ complex near a POPC:POPS(70:30) bilayer. (F-H) Representative protein-lipid contact histograms for States 1, 2 and 3 observed for the apo JAK2-FERM-SH2 near a POPC:POPS:PI(4,5)P_2 (80:10:10) bilayer.

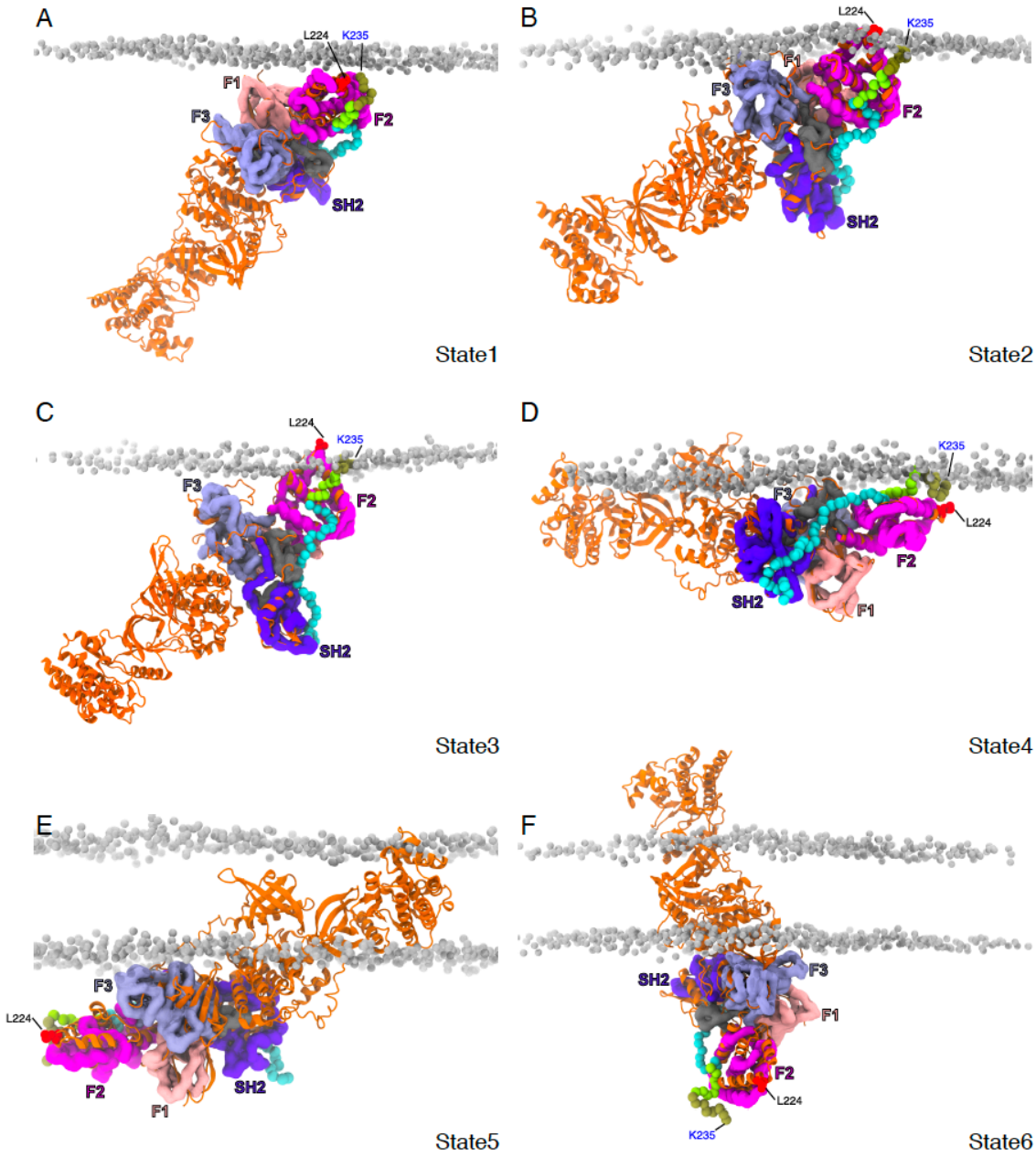

Figure 4 - Figure Supplement 3. Snapshots of the different binding states observed for the JAK2-FERM-SH2 – PRLR-ICD$_{K235-H300}$ complex with the complete structural model of JAK2 (obtained from AF2-EBI database). In each panel the CG JAK2-FERM-SH2 – PRLR-ICD$_{K235-H300}$ complex is depicted and colored as in Fig. 4. The full-length JAK2 model is shown in cartoon representation colored orange. near a POPC:POPS(70:30) bilayer. (F-H) Representative protein-lipid contact histograms for States 1, 2 and 3 observed for the apo JAK2-FERM-SH2 near a POPC:POPS:PI(4,5)P_2 (80:10:10) bilayer.

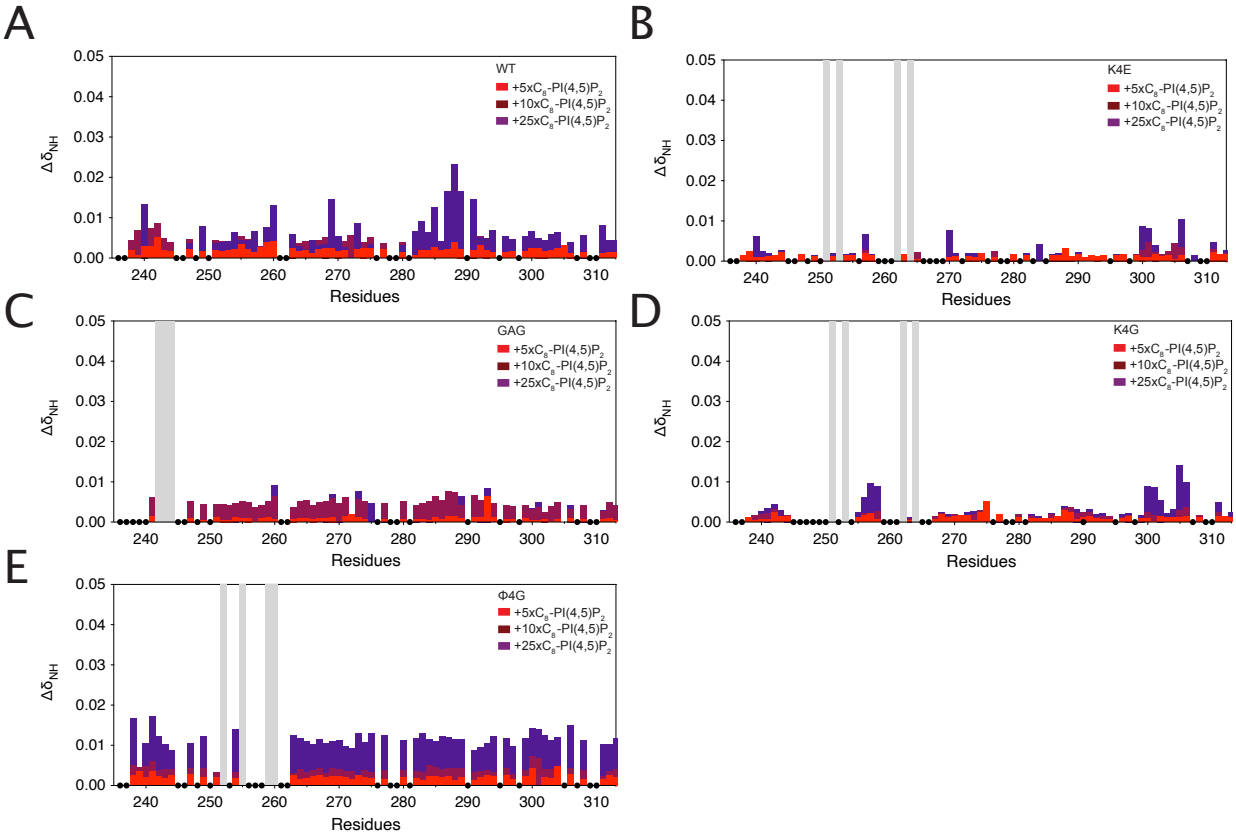

1441

1442 **Figure 5 – Figure supplement** 1: Chemical shift perturbations of $ICD_{K235-G313}$ of A) WT B) K4E, C) GAG, D)
1443 K4G and E) ϕ4G variants.

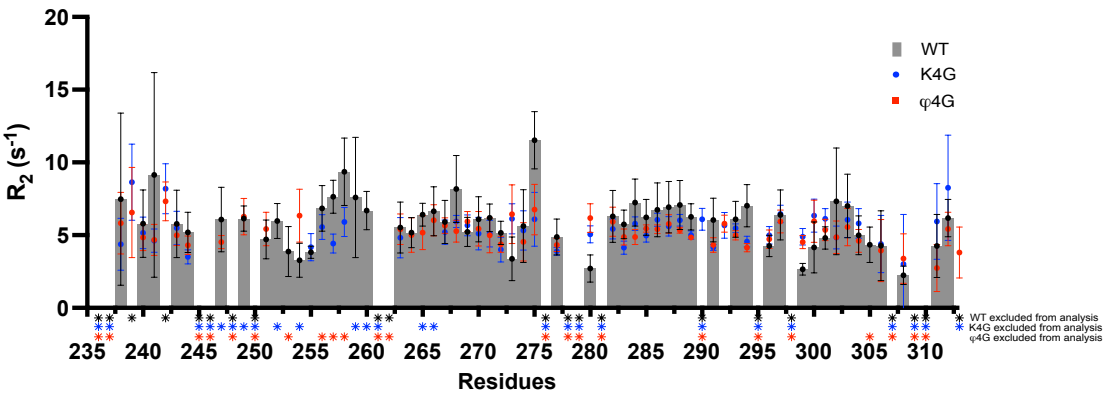

1444

1445 **Figure 5 – Figure supplement** 2: ^{15}N R_2 relaxation rates of $ICD_{K235-G313}$ of WT (grey bars), K4G (blue
1446 dots) and ϕ4G (red squares) variants. Stars indicate signals excluded from the analysis either because it is a

1447 proline, signals are overlapping or a poor exponential fit

1448